ARTICLE IN PRESS

Communications Physics

https://doi.org/10.1038/s42005-026-02493-y

Article in Press

Time-domain field correlation measurements enable tomography of highly multimode quantum states of light

Received: 14 August 2025

Accepted: 2 January 2026

Cite this article as: Hubenschmid, E., Burkard, G. Time-domain field correlation measurements enable tomography of highly multimode quantum states of light. *Commun Phys* (2026). https://doi.org/10.1038/s42005-026-02493-y

Emanuel Hubenschmid & Guido Burkard

We are providing an unedited version of this manuscript to give early access to its findings. Before final publication, the manuscript will undergo further editing. Please note there may be errors present which affect the content, and all legal disclaimers apply.

If this paper is publishing under a Transparent Peer Review model then Peer Review reports will publish with the final article.

ARTICLE IN PRESS

© The Author(s) 2026. **Open Access** This article is licensed under a Creative Commons Attribution 4.0 International License, which permits use, sharing, adaptation, distribution and reproduction in any medium or format, as long as you give appropriate credit to the original author(s) and the source, provide a link to the Creative Commons licence, and indicate if changes were made. The images or other third party material in this article are included in the article's Creative Commons licence, unless indicated otherwise in a credit line to the material. If material is not included in the article's Creative Commons licence and your intended use is not permitted by statutory regulation or exceeds the permitted use, you will need to obtain permission directly from the copyright holder. To view a copy of this licence, visit http://creativecommons.org/licenses/by/4.0/.

ARTICLE IN PRESS

Time-domain field correlation measurements enable tomography of highly multimode quantum states of light

Emanuel Hubenschmid* and Guido Burkard†

Department of Physics, University of Konstanz, D-78457 Konstanz, Germany

Abstract

Recent progress in ultrafast optics facilitates the investigation of the dynamics of highly multimode quantum states of light. Yet, the complete tomographic reconstruction of optical quantum states with prior unknown statistics and dynamics is still challenging, since state-of-the-art tomographic methods require the measurement of orthogonal and distinguishable modes. Here, we propose a tomography scheme based on time-domain quadrature correlation measurements and theoretically demonstrate its ability to reconstruct highly multimode Gaussian states. In contrast to (eight-port) homodyne detection, the two local oscillator pulses are shorter in time and are (independently) time-delayed against the pulsed quantum state. The distinguishable mode structure is obtained in post-processing from the correlation measurement data by orthogonalization. We show that the number of reconstructable modes increases with the number of time delays used and decreases with the temporal extent of the local oscillator. Additionally, we compare dual-pulse homodyne detection and electro-optic sampling. By analysing the (quantum) correlations present in the measurement data, we show how thermalisation of the quantum state during detection leads to the requirement of correlation measurements. Furthermore, we open an avenue to extending our tomography scheme to non-Gaussian states.

ARTICLE IN PRESS

* emanuel.hubenschmid@uni-konstanz.de

† guido.burkard@uni-konstanz.de

ARTICLE IN PRESS

INTRODUCTION

Pulsed quantum states of light [1–3] are vastly complex and rich objects with numerous degrees of freedom – a property which makes these states desirable or even unavoidable for many applications spanning from fundamental investigation of the dynamics of quantum systems [4, 5] to the transmission of quantum information over large distances [6–14] or through quantum networks [15–17]. Full quantum state tomography of the radiation field, i.e., the complete characterization encompassing the statistics of pulsed (free space) quantum states poses a challenge even for state-of-the-art experiments using fast detection [18–21] or mode selection [22–27], since the information describing the state can be distributed among a high number of optical modes.

The complete dynamics of a pulsed quantum state (for some fixed polarization) can be described in a phase space, spanned by the electric-field-related quadrature $\hat{p}_\omega = \frac{\mathrm{i}}{\sqrt{2}}(\hat{a}_\omega^\dagger - \hat{a}_\omega)$ and its conjugate $\hat{x}_\omega = \frac{1}{\sqrt{2}}(\hat{a}_\omega^\dagger + \hat{a}_\omega)$ with (angular) frequency ω and corresponding Bosonic annihilation operator $\hat{a}_\omega$ [28, 29]. Defining a quantum state in the phase space of continuous frequency ω can lead to divergences [30, 31], whereas discretizing the (free space) phase space using a basis of orthogonal functions $f_i(\omega)$ allows one to describe the quantum state by a multimode Wigner function [32, 33]. Since the Fourier transforms $f_i(t)$ of the mode functions allow a description in the time domain, the corresponding modes are called temporal modes [34, 35]. To describe low-frequency and broadband modes, we introduced the subcycle mode basis. The fundamental mode,

$$f_0(\omega) = \left[\frac{2/\sigma_0}{\Gamma(k_0 + 1/2)}\right]^{\frac{1}{2}} \left(\frac{\omega}{\sigma_0}\right)^{k_0} \exp\left(-\frac{\omega^2}{2\sigma_0^2}\right), \tag{1}$$

of the subcycle mode basis is described by the frequency scaling σ_0 and cycle parameter k_0. While the frequency scaling relates to the bandwidth $\Delta\omega_0 \approx \sqrt{2\ln(2)}\sigma_0$ of the fundamental mode, the cycle parameter k_0 determines the number of optical cycles completed during the temporal extent of the pulse. Thus, for a given bandwidth, k_0 determines the central frequency, $\bar{\omega}_0 \approx \frac{\Delta\omega_0}{\sqrt{2\ln(2)}}\sqrt{k_0 + \frac{1}{\pi}}$ of the pulse. The pulse is subcycle for $0 < k_0 \leq 1$, i.e., the duration of the pulse is to short to complete a single optical oscillation. All higher order modes, $f_i(\omega)$, of the subcycle basis are obtained by multiplying the fundamental mode with generalized Laguerre polynomials (see Methods for more details). The orthogonal functions define two sets of orthogonal quadrature operators $\hat{x}_i = \int_0^\infty f_i(\omega)\hat{x}_\omega \mathrm{d}\omega$ and $\hat{p}_i = \int_0^\infty f_i(\omega)\hat{p}_\omega \mathrm{d}\omega$, each pair $(\hat{x}_i, \hat{p}_i)$ acting on the same temporal mode. If we collect the eigenvalues of the operators $\hat{\boldsymbol{\zeta}} = (\hat{x}_0, \hat{x}_1, \ldots, \hat{p}_0, \hat{p}_1, \ldots)^\mathsf{T}$ in a vector $\boldsymbol{\zeta}$, the pulsed quantum state can be represented by the multimode Wigner function $W(\boldsymbol{\zeta})$. For multi-mode Gaussian states, the Wigner function,

$$W(\boldsymbol{\zeta}) = \frac{1}{\sqrt{\det(\mathrm{cov})}} \exp\left[-\frac{1}{2}(\boldsymbol{\zeta} - \boldsymbol{\mu})^\mathsf{T} \mathrm{cov}^{-1}(\boldsymbol{\zeta} - \boldsymbol{\mu})\right], \tag{2}$$

is completely characterized by the expectation value, $\boldsymbol{\mu} = \langle\hat{\boldsymbol{\zeta}}\rangle$, of the quadrature with respect to the quantum state and the (symmetric) covariance matrix cov, with the determinant of the covariance matrix det(cov) [32, 33]. Tomography of optical quantum states is usually accomplished by reconstructing the Wigner function (or a smoothed out, positive phase-space density like the Husimi function), from individual quadrature

ARTICLE IN PRESS

measurements at different directions in phase space [36–41] (or simultaneous measurement of two noncommuting quadratures [42–48]). Quadrature measurements can be implemented using homodyne detection where the quantum pulse to be measured is interfered at a beam splitter with a strong, coherent reference pulse, called local oscillator (LO). The difference between the photon number detected at each output port constitutes a quadrature measurement in the temporal mode defined by the local oscillator pulse [49]. Yet, the reconstruction of the multimode Wigner function $W(\boldsymbol{\zeta})$ would require the measurement of the complete high-dimensional phase-space statistics and even in the Gaussian case of equation (2) would require the measurement of all covariances between temporal modes. One approach is to measure in a quadrature basis for which the covariance matrix cov is diagonal [22–25, 27]. Measuring in the eigenbasis of cov is optimal in the number of measurements required for a complete reconstruction, i.e., for the determination of the variances corresponding to the most significant modes. While being very efficient, this approach requires knowledge of the most significant modes constituting the pulsed quantum state.

In contrast to matching the (temporal) mode of the local oscillator to the quantum state, as described above, recent works have proposed a quantum state tomography in the time domain, accessing the (time local) phase-space dynamics of free-space quantum states with a high temporal resolution [50–53]. Inspired by the electro-optic sampling of vacuum fluctuations [54–60] and pulsed squeezed states [61–63], time-domain quantum state tomography uses an ultrashort local oscillator pulse to sample the phase space statistics of the quantum pulse. By repeating the reconstruction for different time delays between the local oscillator and quantum pulse, the (time-local) dynamics of the quantum state can be scanned through. Electro-optic sampling can be understood as homodyne detection with the local oscillator pulse in a higher frequency range as the sampled state [64–71]. To enable the interference of the high-frequency local oscillator and the lower-frequency state, the state is upconverted to the frequency range of the local oscillator with the aid of a nonlinear interaction. We refer to the coherent pulse involved in the nonlinear interaction as probe and in the subsequent homodyne detection as local oscillator. In our description the probe and local oscillator pulses can differ. In general, the frequency conversion can involve sum-frequency (SF) and difference-frequency (DF) processes [72]. In many cases, the DF processes are suppressed by a wave-vector mismatch between the involved photons; however, they are matched in the subcycle regime and have to be accounted for in electro-optic sampling. The simultaneous presence of both SF and DF processes affects the quadrature correlations generated in the nonlinear interaction [50], similar to the effect of losses during the interaction [73]. In the Supplementary Note 5, we present a approach that still allows the identification of the most significant modes contributing to the nonlinear interaction, even in the non-perturbative regime, for which electro-optic sampling is expected to operate shot-noise free [50]. The advantage of electro-optic sampling compared to homodyne detection is the ability to sample low frequencies, usually in the mid-infrared to THz range, with a broadband probe at optical frequencies, thus approaching a subcycle temporal resolution. In this frequency range, the dynamics is too fast for electronics, but the photon energy is comparable to thermal energies at room temperature, making efficient photo-detection challenging. Therefore, electro-optic sampling and

homodyne detection can be used complementarily, covering a frequency range from microwave to optical, with electro-optic sampling accessing the mid-infrared to THz range [60], filling the gap between the microwave [30, 74] and optical [75, 76] frequency ranges that homodyne detection is available for. Electro-optic sampling has recently been extended to temporal quadrature correlation measurements and applied to the ground state of the electromagnetic field [77–82]. A similar method based on the time-domain correlation measurement method has been applied to investigate magnetic properties exploiting the magneto-optic instead of the electro-optic effect [83]. However, the application of temporal quadrature correlation measurements to more intricate, highly multimode (Gaussian) quantum states of the electromagnetic field is still missing. We fill this gap with our proposal to reconstruct the orthogonal mode structure of pulsed Gaussian quantum states from overlapping time-domain correlation measurements.

In this work, we propose a method, which we term correlation tomography, that only relies on time-domain correlation measurements of two electromagnetic field quadratures. Each of the two quadrature measurements determines the quantum state of the field at an individually controllable time instance. Since any real experiment exhibits a finite bandwidth and thus a finite detection time, the two time windows of the measurement may overlap. The key insight is that the covariances between distinguishable temporal modes of quantum states can be recovered from temporally overlapping correlation measurements by orthogonalizing the overlapping local oscillator states in post-processing. Thus, the proposed method is able to reconstruct the temporal mode structure and the statistics of a pulsed quantum state of light. While the mode basis is determined by the temporal resolution of the measurements, the statistics of the quadrature in this basis is determined by the quantum state. We find that the number of reconstructable modes scales with the bandwidth of the detection and the number of time delays used in the measurement. We compare two implementations of correlation tomography: One based on homodyne detection and one on electro-optic sampling. By optimising the probe pulse used in electro-optic sampling, one can shift the reconstructed modes toward lower frequencies, potentially resolving dynamics below a single optical oscillation and entering the subcycle regime. We analyse signs of (quantum) correlations present in the measurement data obtained from dual-pulse homodyne detection and argue how thermalisation due to entanglement breakage leads to the requirement of correlation measurements even for pure states such as the squeezed vacuum. Furthermore, we open an avenue to the extension to non-Gaussian states by providing the full joint statistics of time-domain quadrature measurements and show how to obtain information about the dynamics of a Fock state occupying a single temporal mode from correlation measurements. The ultrafast measurement of photon-number correlations of two non-overlapping spatial-temporal modes using dual-pulse, phase-averaged homodyne detection has been demonstrated by McAllister and Raymer [84, 85]. While this seminal method allows to obtain higher-order correlation functions, it is restricted to non-overlapping modes. It is still an open question whether the orthogonalization procedure presented in this work combined with the phase-averaged homodyne detection of [84, 85] could be used to obtain higher-order photon-number correlators between more than two temporal modes. Parallel to our work, the reconstruction of Gaussian states has been explored using electro-optic

ARTICLE IN PRESS

sampling in the perturbative regime [86]. This approach starts by deconvolving the measurement statistics and then expands the result in the principle modes, while we propose to first expand the local oscillator states in the mode basis and then invert the measurement statistics by a singular value decomposition, automatically taking care of any numerical instability. The numerical stability is especially relevant for electro-optic sampling, since for some frequency the phase mismatch may result in small contributions to the measurement and thus singularities during the inversion. Overall, we present a numerically stable algorithm able to reconstruct a highly multimode pulsed Gaussian quantum states from field correlation measurements. Furthermore, expanding in the mode basis first allows us to perform a time-domain quantum correlation analysis of multimode squeezed vacuum pulses which motivates the requirement of a correlation measurement. Lastly, we present a possibility to extend the reconstruction to pulsed non-Gaussian states by considering the example of a Fock state.

RESULTS AND DISCUSSION

Time-domain quadrature correlation measurements

The time-domain quadrature correlation measurement we propose is schematically depicted in Fig. 1. To enable correlation measurements, the local oscillator and quantum pulse are subdivided using 50:50 beam splitters and are directed towards two detection arms, which we will refer to as arm a and arm b. The two local-oscillator pulses traverse a delay stage, which adds the time delays Δt_a and Δt_b relative to the pulsed quantum state to the respective local oscillators. Subsequently, the local oscillator and quantum pulse combine in a polarizing beam splitter (PBS) and enter the detection stage.

Each detection stage constitutes a homodyne measurement and can thus be related to a quadrature measurement of the temporal mode defined by the local oscillator. One subtle difference to usual homodyne detection is the orthogonal polarization of the local oscillator and the quantum pulse in the z- and s-direction. This requires a wave plate which shifts the phase of the field polarized along the optical axis of the wave plate by Φ. The optical axis of the wave plate is rotated by θ away from the z-axis around the propagation direction k, to produce interference between the quantum and classical pulse. For the balanced photodetection, a polarizing beam splitter is required to separate the s- and z-polarisation direction. The combined effect of the wave plate and polarizing beam splitter replaces the beam splitter and unrotated wave plate in usual homodyne detection [41, 50]. The wave plate leads to an effective phase shift $\varphi = \varphi(\Phi, \theta)$ of the local oscillator (see Methods). The use of a half-wave plate rotated by 22.5° results in an $\hat{x}$-quadrature measurement with $\varphi = 0$, while choosing a quarter-wave plate rotated by 45° results in a $\hat{p}$-quadrature measurement with $\varphi = \pi/2$. Electro-optic sampling combines a frequency up-conversion in a nonlinear crystal, called detection crystal (DX), with homodyne detection to enable quadrature measurements in the terahertz (THz) frequency range. The nonlinear interaction is gated by a strong coherent pulse, with amplitude α_{DX} for both arms, which we will call the probe pulse. While the probe is polarized along the z-direction,

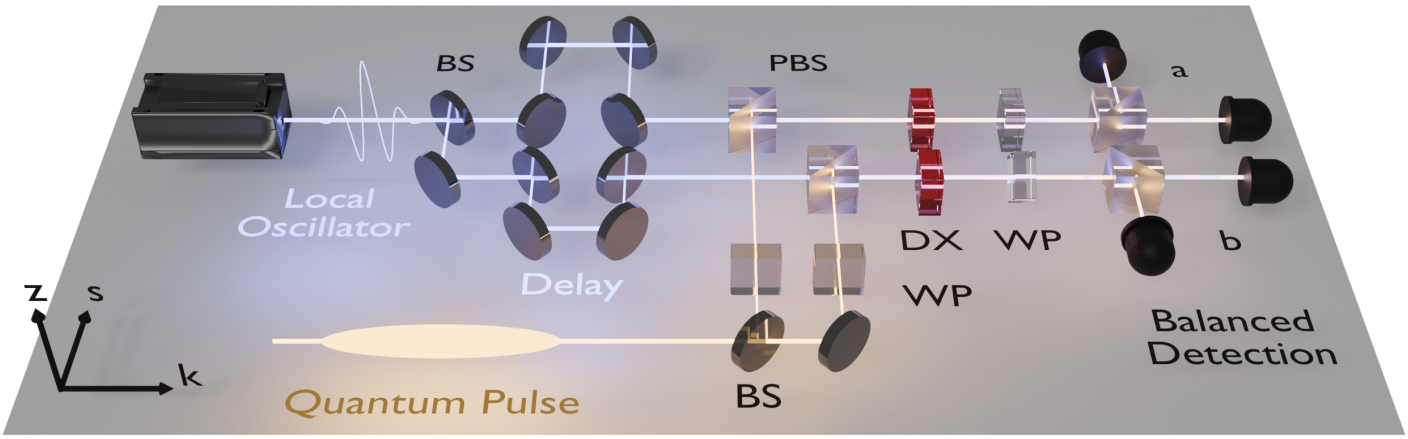

Fig. 1. **Schematic of the proposed quadrature correlation measurement.** The z-polarised, short local oscillator (LO) pulse (blue) and s-polarised quantum pulse (orange) are subdivided by beam splitters (BS) and directed towards the two detection arms referred to as a and b. Before combining in a polarising beam splitter (PBS) with the quantum pulse, each local oscillator pulse traverses a delay stage, adding the time delays Δt_a or Δt_b between the quantum state and LO. If the detection stage is implemented through electro-optic sampling, the quantum pulse is at lower frequencies (usually THz to mid-infrared) than the LO (usually optical frequencies), which is called the probe pulse in this context. The quantum pulse is upconverted to the probe's frequency range by interacting in a nonlinear (detection) crystal (DX). To control the quadrature amplified by the nonlinear crystal, the two parts of the quantum pulse need to pass through wave plates (WP) prior to the nonlinear crystal. Afterwards, the quadrature of the (potentially upconverted) quantum pulse in the temporal mode of the LO is measured by homodyne detection. Different from usual homodyne detection, the quantum and classical pulses are mixed in a wave plate with its optical axis rotated by θ away from the z-axis around the k-direction. A half-wave plate rotated by $\theta = 22.5°$ results in an x-quadrature measurement, while a quarter-wave plate rotated by $\theta = 45°$ yields a p-quadrature measurement. Subsequently, on each detection stage, the s- and z-polarised contributions are separated by a PBS. A balanced photon detection results in a measurement signal that amounts to the difference between the photon numbers in the s- and z-polarisation. If the detection stage is implemented as homodyne detection, the nonlinear crystal is removed.

the quantum pulse is polarized in the s-direction, which is why we introduced the homodyne detection with orthogonal polarizations as inputs. After the nonlinear interaction, the probe pulse can be replaced by a new local oscillator pulse to optimise the detection. Since the nonlinear crystal only amplifies one quadrature, an additional (unrotated) wave plate acting on the quantum pulse between the beam splitter and nonlinear crystals is required, to enable the rotation of the quantum state in phase space by 90°.

The initial state of the local oscillator pulse at detection arm $\xi = a, b$ directly after the first beam splitter, can be represented by the vector $\boldsymbol{\zeta}_{\mathrm{LO}}^{\mathsf{T}}$ in the high-dimensional phase space with respect to the mode basis $f_i(\omega)$ (see Methods for definition). Since all components of the setup in Fig. 1 correspond to a quadratic Hamiltonian, we can describe the time evolution of the initial quadratures $\hat{\boldsymbol{\zeta}}$ using a symplectic transformation, $\hat{\boldsymbol{\zeta}}' = M\hat{\boldsymbol{\zeta}}$ [32, 33]. With only expressions linear in the quadrature operators, $\boldsymbol{\zeta}_{\mathrm{LO}}^{\mathsf{T}}\hat{\boldsymbol{\zeta}}'$, relevant to field quadrature

ARTICLE IN PRESS

measurements, we can equivalently calculate the effective state of the local oscillator $M^{\mathsf{T}}\boldsymbol{\zeta}_{\mathrm{LO}}$. Thus, at the arm $\xi = a, b$ the effective state of the local oscillator for the quadrature measurement is described by the vector $\boldsymbol{\zeta}_{\mathrm{LO}}^{\mathsf{T}}(\Delta t_\xi, \alpha_{\mathrm{DX}}, \varphi_\xi^{\mathrm{tot}}) = M_{\mathrm{WP}}^{\mathsf{T}}(\varphi_\xi^{\mathrm{tot}} - \varphi_\xi) M_{\mathrm{DLY}}^{\mathsf{T}}(\Delta t_\xi) M_{\mathrm{NL}}^{\mathsf{T}}(\alpha_{\mathrm{DX}}) M_{\mathrm{WP}}^{\mathsf{T}}(\varphi_\xi)\boldsymbol{\zeta}_{\mathrm{LO}}$, depending on the phase $\varphi_\xi^{\mathrm{tot}} - \varphi_\xi$ of the unrotated wave plate represented by $M_{\mathrm{WP}}^{\mathsf{T}}(\varphi_\xi^{\mathrm{tot}} - \varphi_\xi)$, the time delay Δt_ξ added by the delay stage, described through $M_{\mathrm{DLY}}(\Delta t)$, the probe amplitude α_{DX} driving the nonlinear interaction, $M_{\mathrm{NL}}^{\mathsf{T}}(\alpha_{\mathrm{DX}})$, and phase φ_ξ added to the local oscillator by the wave plate, $M_{\mathrm{WP}}^{\mathsf{T}}(\varphi_\xi)$. The quadrature measured by the setup is determined by the total angle, $\varphi_\zeta^{\mathrm{tot}}$, which equals the sum of the phase added by each of the two wave plate. In the case of homodyne detection the nonlinear crystal and unrotated wave plate are absent, i.e., $\alpha_{\mathrm{DX}} = 0$ and $\varphi_\xi^{\mathrm{tot}} = \varphi_\xi$. For more details, see Methods.

As a final step to relate the quadrature of the quantum pulse at the input to the quadrature measured by one of the balanced detections, the effect of the beam splitter has to be considered. While one input port of the beam splitter is occupied by the pulsed quantum state (with quadrature operators $\hat{\boldsymbol{\zeta}}$), the other input port couples to the vacuum (with quadrature operators $\hat{\boldsymbol{\zeta}}_{\mathrm{vac}}$). The vacuum at the empty port leads to additional noise to the detected photon-count difference. This additional noise is fundamentally unavoidable in the simultaneous detection since it ensures the positivity of the probability distribution over the photon-difference counts [41, 50]. Thus, the detection arm $\xi = a, b$ measures the quadrature,

$$\hat{q}_\xi(\Delta t_\xi, \alpha_{\mathrm{DX}}, \varphi_\xi^{\mathrm{tot}}) = \boldsymbol{\zeta}_{\mathrm{LO}}^{\mathsf{T}}(\Delta t_\xi, \alpha_{\mathrm{DX}}, \varphi_\xi^{\mathrm{tot}})\hat{\boldsymbol{\zeta}} + \boldsymbol{\zeta}_{\mathrm{LO}}^{\mathsf{T}}(\Delta t_\xi, \alpha_{\mathrm{DX}}, \varphi_\xi^{\mathrm{tot}} + \Delta\varphi_\xi)\hat{\boldsymbol{\zeta}}_{\mathrm{vac}}. \tag{3}$$

Here we have assumed a uniform 50:50 beam splitter over all frequencies. While this assumption might hold for the broadband quantum state, the even broader local oscillator could violate this assumption. However, by expanding the time-evolution of a non-uniform beam splitter in the mode basis $f_i(\omega)$, one can account for this effect. The above equation can be understood as projecting the high-dimensional, *s*-polarized quadrature operators $\hat{\boldsymbol{\zeta}}$ and $\hat{\boldsymbol{\zeta}}_{\mathrm{vac}}$ at the inputs of the beam splitter onto the transformed local oscillator state. The additional phase $\Delta\varphi_a = \pi/2$ for detection arm *a* and $\Delta\varphi_b = -\pi/2$ for arm *b* is due to the phase shift acquired in the reflection at the beam splitter. The phase is on the vacuum port since $\varphi_\xi^{\mathrm{tot}}$ is already adjusted to the reflection phase shift (see Methods). Equation (3) is only valid for a large local oscillator amplitude. We assume the amplitude of the two probes both equal $\alpha_{\mathrm{DX}} \neq 0$ in the case of electro-optic sampling and $\alpha_{\mathrm{DX}} = 0$ for homodyne sampling.

Reconstruction of highly multimode Gaussian quantum states

To gain statistical information about the sampled quantum state and its dynamics, different combinations of time delays in the two detection arms of the setup in Fig. 1 have to be measured. Yet, the statistical information contained in the covariance matrix, cov, of the pulsed quantum state is encoded in orthogonal, distinguishable modes, while the local oscillator pulses at different time delays can overlap and are thus partially indistinguishable. We present an algorithm capable of extracting information about the orthogonal

mode structure of the pulsed quantum state from the correlation measurements. The algorithm contains the following steps:

1. Perform a field quadrature correlation measurement, as described above, for all possible combinations, $i, j \in \mathbb{N}_{\leq 2N}$, of parameter settings $(\Delta t_a, \alpha_{\mathrm{DX}}, \varphi_a^{\mathrm{tot}}) = \Gamma_i$ at arm a and $(\Delta t_b, \alpha_{\mathrm{DX}}, \varphi_b^{\mathrm{tot}}) = \Gamma_j$ at arm b, taken from the series

$$\Gamma = \Big((\Delta t_1, \alpha_{\mathrm{DX}}, 0), (\Delta t_2, \alpha_{\mathrm{DX}}, 0), \ldots, (\Delta t_1, \alpha_{\mathrm{DX}}, \pi/2), (\Delta t_2, \alpha_{\mathrm{DX}}, \pi/2), \ldots \Big), \tag{4}$$

of N time delays $(\Delta t_i)_{i \leq N} = \{\Delta t_1, \Delta t_2, \ldots, \Delta t_N\}$ and two possible wave plate settings $\varphi_\xi^{\mathrm{tot}} = 0, \pi/2$. Collect all the measurement results for the different time delays and wave plate settings in the correlation matrix

$$\mathrm{corr}_{i,j} = \frac{1}{2} \left\langle \{ \hat{q}_a(\Gamma_i), \hat{q}_b(\Gamma_j) \} \right\rangle , \tag{5}$$

where the quadrature operators $\hat{q}_\xi$ are defined in equation (3) and $\{\hat{A}, \hat{B}\} = \hat{A}\hat{B} + \hat{B}\hat{A}$ denotes the anticommutator.

2. The states of the local oscillators for the corresponding measurements in the first step are assembled in the matrix

$$Z_{\mathrm{LO}} = (\zeta_{\mathrm{LO}}(\Gamma_i) \;\mid\; i \leq 2N). \tag{6}$$

3. Use the definitions in equation (3)-(6) to relate the covariance matrix of the pulsed quantum state, $\mathrm{cov}_{\hat{\rho}}$, as well as the covariance matrix of the vacuum at the empty input port of the beam splitter, $\mathrm{cov}_{\mathrm{vac}} = \frac{1}{2}\mathbb{I}$ ($\mathbb{I}$ being the identity matrix), to the covariance matrix of the measurement results,

$$\mathrm{corr} = Z_{\mathrm{LO}}^{\mathsf{T}} \, \mathrm{cov}_{\hat{\rho}} \, Z_{\mathrm{LO}} - Z_{\mathrm{LO}}^{\mathsf{T}} \, \mathrm{cov}_{\mathrm{vac}} \, Z_{\mathrm{LO}}. \tag{7}$$

Orthogonalise the local oscillator states and transform the correlation matrix with the aid of the singular value decomposition, $Z_{\mathrm{LO}} = U \Sigma V^{\mathsf{T}}$, and the Moore-Penrose pseudoinverse [87, 88] of Σ, denoted by Σ^+. We define the diagonal projector $P = \Sigma\Sigma^+$ and the transformed covariance matrix $\mathrm{cov}_{\hat{\rho},U} = U^{\mathsf{T}} \, \mathrm{cov}_{\hat{\rho}} \, U$. After subtracting the vacuum contribution and transforming equation (7) with $V\Sigma^+$, we get the (partially) reconstructed covariance matrix

$$P \, \mathrm{cov}_{\hat{\rho},U} \, P = \left[V\Sigma^+ \right]^{\mathsf{T}} \mathrm{corr} \, V\Sigma^+ + \frac{1}{2} UPU^{\mathsf{T}}. \tag{8}$$

To avoid numerical instability, we set all singular values of the matrix Z_{LO} to zero if they are smaller than 10^{-3} times the maximal singular value.

We provide an implementation of the algorithm in Python [89]. The matrix U used in the last step of the algorithm needs to be symplectic to ensure that the reconstructed covariance matrix corresponds to a valid quantum state. However, it is always possible to find such a symplectic U since the two wave plate settings

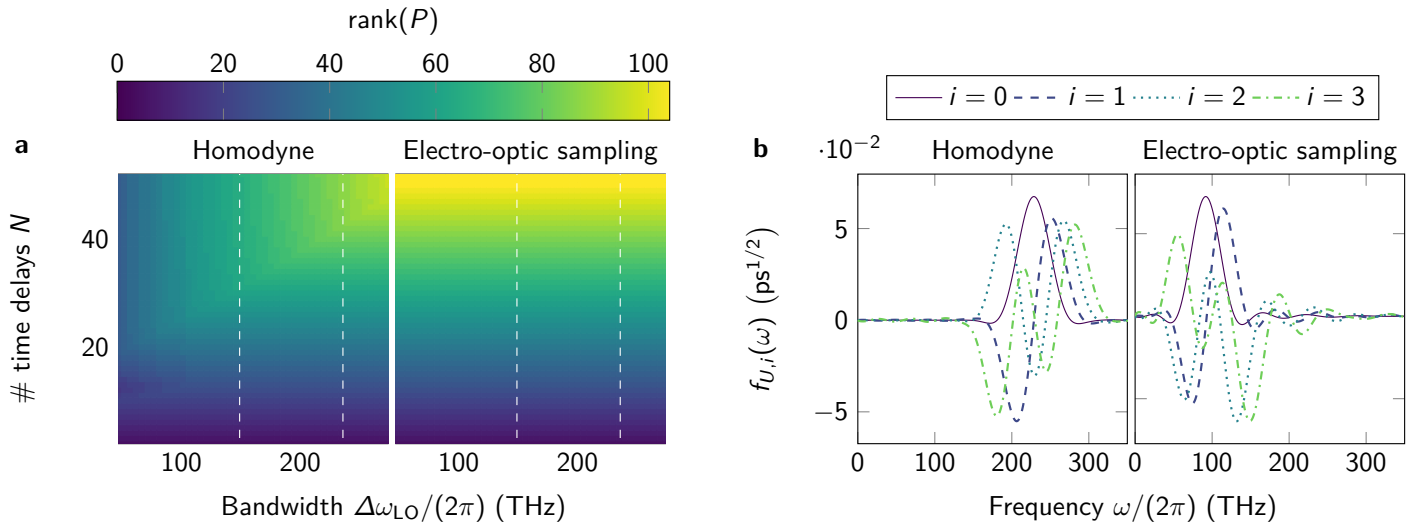

Fig. 2. **Temporal resolution and reconstructed mode basis. a**, Number of (temporal) modes, given by rank(P), reconstructed with the algorithm presented in the main text in dependence of the local oscillators bandwidth $\Delta\omega_{\mathrm{LO}}$ and the number of time delays N used in the correlation measurements for homodyne detection and electro-optic sampling respectively. The centre of the local oscillator pulse is fixed at $\bar{\omega}_{\mathrm{LO}}/(2\pi) = 230\,\mathrm{THz}$ and the vertical dashed lines indicate the transition from multicycle to single cycle ($k_{\mathrm{LO}} = 3$) and to subcycle pulses ($k_{\mathrm{LO}} = 1$). **b**, First four (orthogonalized) mode functions in the frequency domain reconstructed by the correlation measurement. In the case of homodyne detection, the bandwidth of the local oscillator is $\Delta\omega_{\mathrm{LO}}/(2\pi) = 59\,\mathrm{THz}$ and thus multicycle with $k_{\mathrm{LO}} = 20.8$. For electro-optic sampling, the probe involved in the nonlinear interaction is centred at $\bar{\omega}_{\mathrm{DX}}/(2\pi) = 200\,\mathrm{THz}$ with the bandwidth $\Delta\omega_{\mathrm{DX}} = 118\,\mathrm{THz}$ ($k_{\mathrm{LO}} = 4$), but is filtered after the nonlinear interaction to $\bar{\omega}_{\mathrm{LO}}/(2\pi) = 230\,\mathrm{THz}$ and$\Delta\omega_{\mathrm{LO}}/(2\pi) = 59\,\mathrm{THz}$.

exchange the role of the x- and p-quadrature, therefore the x- and p-quadrature blocks of Z_{LO} possess the same singular value decomposition. In the case of electro-optic sampling, the phase φ_ξ is fixed by the choice of quadrature amplified by the nonlinear interaction. Thus, the quantum pulse needs to pass an additional (unrotated) $(\varphi_\xi^{\mathrm{tot}} - \varphi_\xi)$-wave plate prior to the beam splitter in order to amplify the other quadrate and enable the decomposition using a symplectic matrix U. In general, the reconstructed covariance matrix in equation (8) corresponds to the marginal distribution of a Gaussian state with covariance matrix $\mathrm{cov}_{\hat{\rho},U}$. Thus, the rank $r = \mathrm{rank}(P)$ of the projector determines the dimension of the phase space reconstructable from the measurement data. The number of reconstructable phase space dimensions increases with the number of time delays N and the bandwidth $\Delta\omega_{\mathrm{LO}}$ of the local oscillators, as shown in Fig. 2 **a** for the case of homodyne detection ($\alpha_{\mathrm{DX}} = 0$) and electro-optic sampling ($\alpha_{\mathrm{DX}} = -1.95 \cdot 10^6$, optimised according to Supplementary Note 5). We assume an equal temporal distribution of the time delays $(\Delta t_i)_{i\leq N}$ over the time interval $I_{\Delta t} = [-12\,\mathrm{fs}, 12\,\mathrm{fs}]$ in the case of homodyne detection and $I_{\Delta t} = [-17\,\mathrm{fs}, 17\,\mathrm{fs}]$ for electro-optic sampling. The corresponding orthogonalized (local oscillator) mode functions, $f_{U,i}(\omega)$, are obtained from the rows of U, introduced in step 3 of the algorithm, and are shown in Fig. 2 **b**. In the case of homodyne detection, the

ARTICLE IN PRESS

number of reconstructable modes increases linearly with the number of time delays until reaching a plateau. A behaviour explained by Fig. 3 **a** and **c**. As the time delay changes, the vector describing the state of the local oscillator moves along spirals through the high-dimensional phase space, spanned by the rows of U. The vectors describing the local oscillators at two different time delays are linearly independent and, in principle, orthogonalizable. Yet, if the difference in time delay is small, then the vectors are almost linearly dependent, as is the case in Fig. 3 **a** for $\Delta t = 0\,\mathrm{fs}$ and $\Delta t = 0.12\,\mathrm{fs}$. The cutoff introduced at the end of the third step of the algorithm will parallelise these vectors. The cutoff explains the plateau in Fig. 2 **a** and can only be increased by increasing the bandwidth of the local oscillator. A local oscillator shorter in time can resolve more features of the orthogonal mode basis, as evident from Fig. 3 **b** and **d** by considering the overlap from the local oscillator and the orthogonal modes in the time domain. In electro-optic sampling, the modes are centred at much lower frequencies reaching the mid-infrared (MIR) range due to the frequency conversion in the nonlinear crystal, as evident from Fig. 2 **b** and thus can reach a few- up to subcycle resolution as visible in Fig. 3 **d**. This frequency range is particularly interesting. While homodyne detection is available for higher or lower frequencies, the lack of efficient photo detectors makes homodyne detection unsuitable for this frequency range. Another striking feature of Fig. 2 **a** is the dependence of the reconstructed phase space dimension on the bandwidth of the local oscillator in the case of electro-optic sampling. The nonlinear interaction correlates a broad band of frequencies to the detected ones, making the signal resilient to losses due to filtering [26, 50, 90]. This band only weakly depends on the bandwidth of the local oscillator. Thus, the bandwidth of the detection can be much smaller than the sampled frequency range. In the Supplementary Note 5 we show how to choose optimised parameters to correlate the lower frequency modes to the detected ones. The time domain picture in Fig. 3 also shows the different time scales of the dynamics captured by homodyne detection and electro-optic sampling.

As a final remark, we would like to mention that this approach is not limited to time-delayed pulses. In principle, any set of linearly independent pulses, in the time or frequency domain, can be used.

Analysing correlations in the time domain

In the remainder of this article, we will only consider field correlation measurements based on homodyne detection. However, all concepts presented in the following translate to electro-optic sampling. In this section we argue that time local sampling, as done for classical, coherent pulses in time-domain spectroscopy, is not sufficient for quantum states, since correlations prevent the reconstruction of the complete quantum pulse from individual time-local measurements. We begin with the observation that time-local phase-sensitive measurements are insufficient to reconstruct thermal states since they do not carry any phase information. The same argument cannot be made for the squeezed vacuum, since the variance depends on the phase and, in turn, on time. Yet, in the following, we show that squeezed states appear thermalised in a time-domain measurement due to entanglement breaking between measured and unmeasured modes, leading to the

ARTICLE IN PRESS

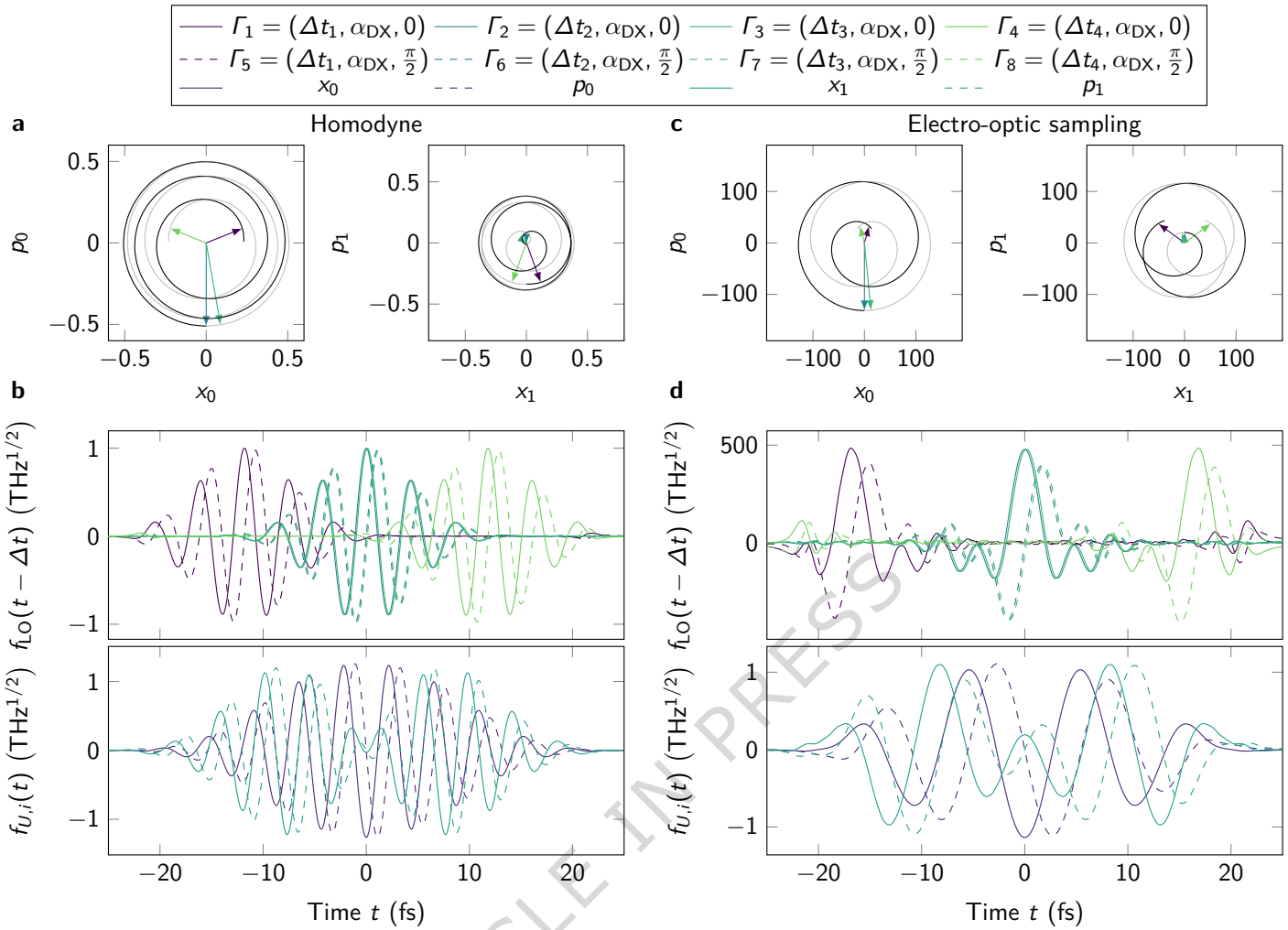

Fig. 3. **Dynamics of the local oscillator in phase space and in the time domain.** **a**, State of the local oscillator for different time delays, $(\Delta t_i)_{i=1,2,3,4} = (-11.76\,\text{fs}, 0.00\,\text{fs}, 0.12\,\text{fs}, 11.76\,\text{fs})$, in the phase space spanned by the first two orthogonalized modes obtained from a homodyne measurement, $\alpha_{DX} = 0$, with a quarter-wave plate. The black (gray) line indicates the evolution for negative (positive) time delays. **b**, Waveform of the time-delayed local oscillator, $f_{LO}(t)$, and first two orthogonalized modes. $f_{U,i}(t)$, obtained from homodyne detection, in the time domain. The symmetric function corresponds to the $\hat{x}$ quadrature, while the antisymmetric function relates to the $\hat{p}$ quadrature. The dynamics in **a** can be obtained from the overlap of the time-delayed local oscillator and the orthogonal quadrature basis. **c**, Phase space representation of the local oscillator with $(\Delta t_i)_{i=1,2,3,4} = (-16.66\,\text{fs}, 0.00\,\text{fs}, 0.17\,\text{fs}, 16.66\,\text{fs})$, in electro-optic sampling after the nonlinear interaction (see Supplementary Note 5.). **d**, Time-domain picture of the effective time-delayed local oscillator and the first two corresponding orthogonalized modes, if electro-optic sampling, $\alpha_{DX} = -1.95 \cdot 10^6$, is used in place of homodyne detection. Due to the frequency conversion of the nonlinear crystal the effective local oscillator, described by $\boldsymbol{\zeta}_{LO}(\Gamma_i)$ in equation (3), is much broader in and centred at lower frequencies as the actual detection. The parameters for the probe and local oscillator pulse are the same as in Fig. 2.

ARTICLE IN PRESS

requirement of correlation measurements for the reconstruction of multimode squeezed states. We assume that the pulsed squeezed state is generated by squeezing the vacuum using a nonlinear interaction equivalent to the one used for electro-optic sampling (see Supplementary Note 6). The strength of the squeezing interaction is determined, among other parameters, by the photon-number content of the pump $N_{\mathrm{GX}} = |\alpha_{\mathrm{GX}}|^2$, with α_{GX} being the coherent amplitude. The average $\hat{x}\hat{x}$-signal for a measurement with two half-wave plates, i.e., $g(\Delta t_a, \Delta t_b, 0, 0) = \langle \hat{q}_a(\Delta t_a, 0, 0)\hat{q}_b(\Delta t_b, 0, 0)\rangle$, for a weakly squeezed state with $\alpha_{\mathrm{GX}} = 2 \cdot 10^3$ is shown in Fig. 4 **a**. The signal is dominated by alternating squeezing and antisqueezing along the time-local axis, i.e., $\Delta t_a = \Delta t_b$. The maxima of the signal are shifted along this axis, which originates from the frequency oscillations of the phase matching function [50]. As the pump strength is increased from $\alpha_{\mathrm{GX}} = 2 \cdot 10^3$ via $\alpha_{\mathrm{GX}} = 3 \cdot 10^4$ to $\alpha_{\mathrm{GX}} = 7 \cdot 10^5$, oscillations along the orthogonal axis, $\Delta t_a = -\Delta t_b$, appear. These oscillations along the time-nonlocal axis are a sign of thermalisation, as a comparison with the signal of a thermal state in Fig. 4 **e** illustrates (see Supplementary Note 9 for details).

The thermalisation of the detected state can be validated with the von Neumann entropy (VNE) shown in Fig. 4 **b**. We define the detected state via the covariance matrix of the observable

$$\mathbf{q} = \frac{1}{\sqrt{2}\|\zeta_{\mathrm{LO}}(0,0,0)\|}(\hat{q}_a[\Delta t_a, 0, 0], \hat{q}_a[\Delta t_a, 0, \pi/2], \hat{q}_b[\Delta t_b, 0, 0], \hat{q}_b[\Delta t_b, 0, \pi/2])^{\mathrm{T}}, \tag{9}$$

the Wigner function of which corresponds to a valid quantum state. Since the initial state is assumed to be pure and the evolution unitary, a finite von Neumann entropy can only originate from entanglement between the detected and undetected parts of the quantum state. The presence of entanglement in the detected state can be determined using the logarithmic negativity (see Methods), shown in Fig. 4 **c**. We chose the bipartition of the detected state to be between the two detection arms $\xi = a, b$. The logarithmic negativity results from an interplay between entanglement within and purity of the quantum state. For weak squeezing, the entanglement and thermalisation (quantified by the von Neumann entropy in Fig. 4 **b**) are low, resulting in a small logarithmic negativity. Increasing the squeezing, the entanglement will increase as well, which in turn leads to more thermalisation, increasing the logarithmic negativity until thermalisation overshadows the entanglement and the logarithmic negativity drops to zero. However, the quantum correlations of the thermalised state can still be captured by the quantum discord (see Methods), even in the presence of thermalisation, and shows a clear increase with the squeezing strength, as can be seen in Fig. 4 **d**. Since the quantum correlations are low in the weak squeezing limit, the signal can be understood as a time-varying noise pattern along the time local axis, $\Delta t_a = \Delta t_b$ (see Supplementary Notes 7 and 8). For stronger squeezing the quantum nature of the multimode squeezed state becomes relevant and correlation measurements are necessary. Fig. 4 **f** shows the von Neumann entropy of the detected state at $\Delta t_a = \Delta t_b = 0$, at which point the local oscillator is matched best to the quantum pulse, as a function of the parameters describing the mode of the local oscillator, i.e., the centre frequency $\bar{\omega}_{\mathrm{LO}}$ and the bandwidth $\Delta\omega_{\mathrm{LO}}$. The minimum of the von Neumann entropy in Fig. 4 **f**, corresponds to the local oscillator mode matched closest to the first principal mode of the squeezed state (see Supplementary Note 6). Yet, in time-domain sampling, the modes of the local oscillator and quantum state are never matched since the detection is faster than the dynamics of the

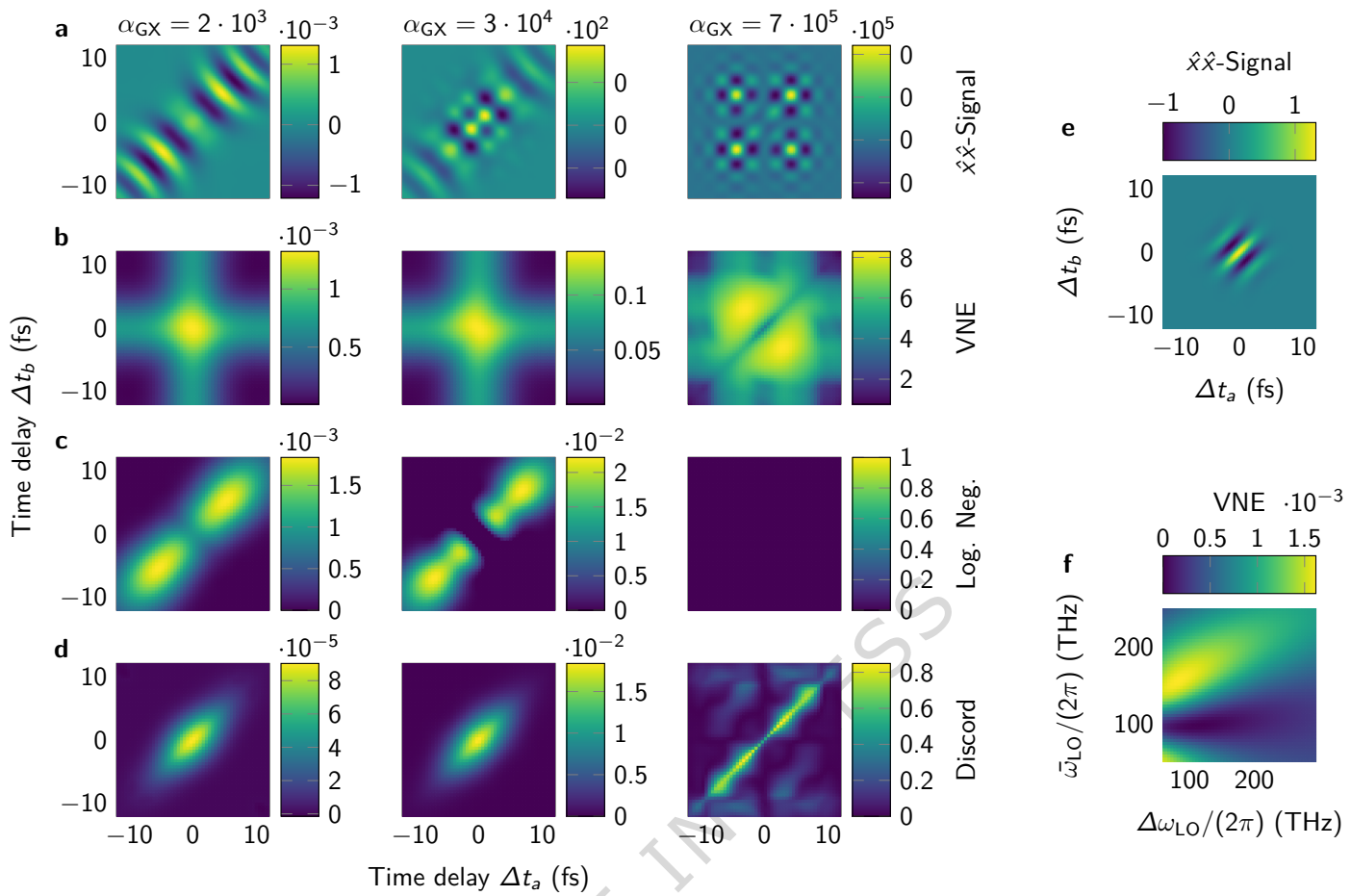

Fig. 4. **Correlations in the sampled state. a**, Correlated signal, $g(\Delta t_a, \Delta t_b, 0, 0) = \langle \hat{q}_a(\Delta t_a, 0, 0)\hat{q}_b(\Delta t_b, 0, 0)\rangle$, for a $\hat{x}\hat{x}$-quadrature measurement, based on homodyne detection, as a function of the time delays Δt_a and Δt_b on the two detection arms a and b, for a weakly squeezed state, $\alpha_{GX} = 2 \cdot 10^3$, moderately squeezed, $\alpha_{GX} = 3 \cdot 10^4$, and strongly squeezed state, $\alpha_{GX} = 7 \cdot 10^5$. The squeezing is implemented by the same free-space nonlinear interaction used in Fig. 1 (see Supplementary Note 6). **b**, Von Neumann entropy (VNE) of the detected state defined by all 16 (co-)variances of the two possible wave-plate settings at the two arms, i.e., quarter- and half-wave plate, and given time delays Δt_a and Δt_b. The input states are the same squeezed states as in **a**. **c**, Entanglement between the two detection arms quantified by the logarithmic negativity of the detected state, described above, with the bipartition between the two detection arms a and b. **d**, Quantum correlations, beyond the entanglement in **c**, quantified by the quantum discord with the bipartition as above. **e**, Correlated signal for $\hat{x}\hat{x}$-quadrature measurement for a thermal state with temperature $T = 1000\,\mathrm{K}$ (see Supplementary Note 9). **f**, Von Neumann entropy of the strongly squeezed state at fixed time delays $\Delta t_a = \Delta t_b = 0$ as a function of the two parameters of the local oscillator, i.e., the bandwidth $\Delta\omega_{LO}$ and centre frequency $\bar{\omega}_{LO}$.

ARTICLE IN PRESS

state, leading to the breakage of entanglement and in turn to thermalisation of the detected state. Therefore, the reconstruction of the (thermalised) multimode quantum state requires correlation measurements, at least in the strong squeezing regime in which thermalisation becomes relevant.

Correlations measurements of non-Gaussian states

Since Gaussian states are completely described by their expectation values and covariance matrix, two-point correlation measurements can fully characterize even highly multimode Gaussian states. Non-Gaussian states such as Fock states, on the other hand, can exhibit higher-order correlations and require going beyond the second moment. In the following, we will provide the joint probability distribution of the correlation measurement and show how to obtain not only statistical, but also dynamical information about the quantum state, even if they are rotationally symmetric in phase space, such as the Fock states. The joint probability distribution,

$$\mathrm{Prob}(x_a, p_b) = \int \dots \int_{-\infty}^{\infty} K(x_a, p_b|\boldsymbol{\zeta}) W(\boldsymbol{\zeta}) \mathrm{d}^{2i_{\max}}\zeta, \tag{10}$$

of the correlated quadrature measurement with outcomes x_a for $\hat{q}_a(\Delta t_a, 0, 0)$ and p_b for $\hat{q}_b(\Delta t_b, 0, \pi/2)$ is given by convolving the $2i_{\max}$-dimensional, multimode Wigner function $W(\boldsymbol{\zeta})$, describing the pulsed quantum state with a multivariate Gaussian kernel $K(x_a, p_b|\boldsymbol{\zeta})$ defined in equation (31), accounting for the effect of the measurement (for details see the Supplementary Note 10). Generally, inverting equation (10) is a nontrivial task. However, in the case of a Gaussian Wigner function, we can recover equation (7) from the convolution, the inversion of which is demonstrated in equation (8). Another example for which equation (10) proves useful is the reconstruction of n-photon Fock states. Figure 5 **a** shows the result of the convolution in equation (10) for a single-mode, three-photon Fock state.

We can distinguish between two special cases of the joint probability distribution by scrutinising the two singular values σ_q with $q = x, p$, quantifying the measurement and preparation uncertainty along two orthogonal directions in the phase space of the Fock state (see Supplementary Note 10 for more details). The singular values σ_q are shown in Fig. 5 **b** as a function of the time delay Δt_b.

In the first case, the two singular values, and thus the measurement uncertainties, are equal, $\sigma_x \approx \sigma_p$. In this case, the two quadrature measurements are maximally incompatible and the measurement statistics are determined by a phase space distribution. If the mode functions of the local oscillator and the pulsed quantum state are matched, the singular values approach 4, $\sigma_q \to 4$, and the phase space distribution converges to the Husimi function of the quantum pulse. Equal measurement uncertainties can be observed along the time local (tl) axis with $\Delta t_a = \Delta t_b$. The Fock state appears to the detection as an incoherent mixture of Fock states with occupations 0 to n distributed binomially, with probability $p = \sigma_q/4$, reproducing the result obtained by time-local quantum state tomography [50].

In the second case, one singular value tends to 2, while the other stays above 2. In this case, the measurement uncertainty of one measurement is decreased at the expense of the other measurement, resulting

ARTICLE IN PRESS

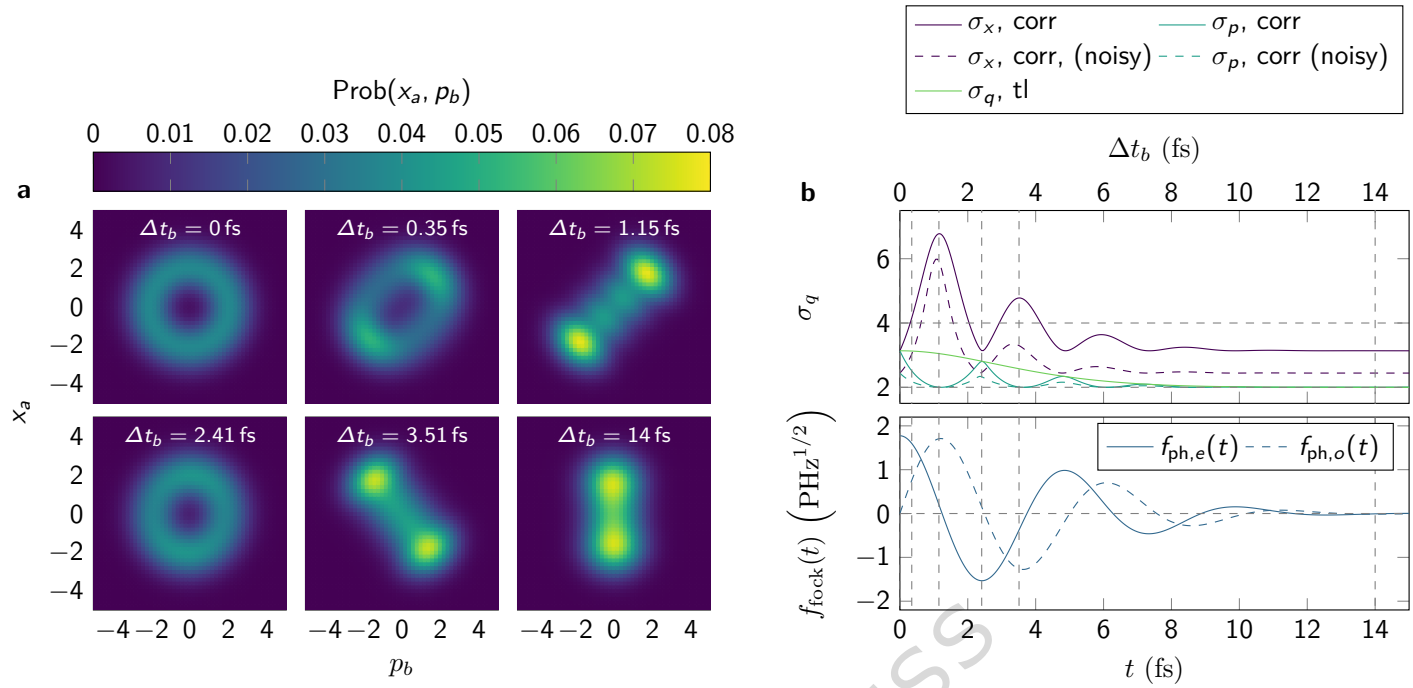

Fig. 5. **Joint probability distribution for correlation measurements of a Fock state.** **a**, Joint probability distribution for a $\hat{x}$-quadrature measurement at detection arm a and a $\hat{p}$-quadrature measurement at detection arm b with fixed time delay $\Delta t_a = 0$ and different Δt_b for each distribution. The joint probability distribution is taken over the possible measurement outcomes, which are the eigenvalues x_a and p_b of the operators $\hat{q}_a(\Delta t_a, 0, 0)$ and $\hat{q}_b(\Delta t_b, 0, \pi/2)$. The input state used in this example is a three-photon Fock state in a temporal mode centred at $\bar{\omega}_{\mathrm{ph}} = 200\,\mathrm{THz}$ with a bandwidth $\Delta\omega_{\mathrm{ph}} = 59\,\mathrm{THz}$. The local oscillator is characterized by $\bar{\omega}_{\mathrm{LO}} = 230\,\mathrm{THz}$ and $\Delta\omega_{\mathrm{LO}} = 118\,\mathrm{THz}$. **b**, The singular values σ_q with $q = x, p$ quantify the compatibility of the two measurements compared to the waveform $f_{\mathrm{ph},e}(t)$ and $f_{\mathrm{ph},o}(t)$ related to the $\hat{x}$ and $\hat{p}$ quadratures of the pulsed Fock state. For a time local (tl) measurement, $\Delta t_a = \Delta t_b$, or for a difference between the time delays equal to integer multiple of half an optical cycle of the quantum states waveform, the singular values are equal $\sigma_x \approx \sigma_p$ and the measurement is incompatible leading to a measurement of the Husimi function, e.g., for $\Delta t_b = 0\,\mathrm{fs}$ or $\Delta t_b = 2.47\,\mathrm{fs}$. For a correlation (corr) measurement with a difference between the time delays equal to odd multiples of a quarter optical cycle, one of the singular values approaches 2. In this case, the same quadrature is measured by both detection arms and the measurements are compatible. The compatibility of the measurement allows the extraction of phase information about the, rotationally symmetric, Fock state. The effect of detectors with a quantum efficiency of $\eta = 0.5$ is shown as dashed coloured lines, labelled σ_x, corr, (noisy) and σ_p, corr, (noisy).

in a smoothed-out quadrature distribution. An example of this special case can be observed at large differences in time delay, one detection arm measures the vacuum and the other (partially) the Fock state. In this case, the probability distribution disintegrates into the quadrature distribution of the vacuum and the Fock state, given by a Hermite-Gauss polynomial, convolved with a Gaussian describing the vacuum contributions from the empty beam splitter port.

Neither case reveals any phase information about the quantum state. However, the singular values σ_q for correlation (corr) measurements oscillate with twice the carrier frequency of the quantum pulse, as shown in Fig. 5 **b**. At a difference between the time delays corresponding to even multiples of a quarter optical cycle of the quantum pulse, orthogonal quadratures of the quantum pulse are measured and the singular values are equal. At a difference between the time delays corresponding to odd multiples of a quarter optical cycle, the same quadrature is measured and one singular value tends to 2. As one of the time delays is varied while the other one is fixed, the measurement statistics interpolates between the two cases and oscillates with twice the carrier frequency of the quantum pulse, as can be seen in Fig. 5 **b**. The oscillation between compatible and incompatible measurements allows the extraction of spectral information about the pulsed Fock states.

There are two effects which could negatively influence the reconstruction of the quantum state. First, a finite quantum efficiency, η, of the detectors used in the balanced detection. While for Gaussian states the noise due to finite quantum efficiency can be subtracted from the variance of the measurement data, in the case of non-Gaussian states we need to include the noise into the calculation. Following Leonhardt and Paul [38], we can calculate the singular values σ_x and σ_p as shown in Fig. 5 **b** for $\eta = 0.5$ in dashed lines. Overall the σ_x and σ_p with finite quantum efficiency are always below the ideal ones, thus the statistics in phase space as well as the dynamics seen in σ_q are washed out. However, photo detectors in the optical frequency can achieve quantum efficiencies well above $\eta = 0.5$ [19]. Second, the phase-space statistics also becomes washed out if the mismatch between the mode of the local oscillator and the Fock state is increased. Additionally, the dynamics of σ_q may deviate more strongly. Including the mode mismatch, quantum efficiencies above 50% are reachable [19] and sufficient to reconstruct Wigner negativity of single photons [91]. While the local oscillator and Fock state mode are not matched in the example of Fig. 5, the oscillation of the incompatibility clearly follow the Fock states temporal mode. Using the dynamical information extracted from Fig. 5 **b**, the local oscillator mode can be matched to the Fock states mode adaptively, improving the reconstruction of the quantum state and thus iteratively approaching the actual quantum state. This is a general feature of any measurement: The more prior information ia available, the better the experiment can be tailored to the measured system and one can thus obtain a more precise measurement result. We chose the example of three photons here to clearly exemplify the shape of the Hermite-Gauss polynomials at $\Delta t_b = 1.15\,\mathrm{fs}$.

CONCLUSION

While time-domain quadrature correlation measurements have already been used to scrutinise the statistics of the ground state of the electromagnetic field, the reconstruction of (unknown) pulsed quantum states has not been addressed to this point. Here, we present a full quantum state tomography scheme able to reconstruct highly multimode Gaussian quantum states. Different from existing tomography schemes, our proposed reconstruction only relies on time-delayed pulses, which are orthogonalised in post-processing. We compare two implementations of the correlation measurement, one based on homodyne detection suited for

ARTICLE IN PRESS

multicycle modes in microwave or optical frequencies and another, based on electro-optic sampling suited for subcycle modes in the THz to mid-infrared frequency range. Accompanying the latter, we develop a non-perturbative description of electro-optic sampling which allows to optimise the probe strength in the strong interaction regime. Furthermore, we show how thermalisation during the detection makes correlation measurements necessary, by analysing the sign of quantum correlations in the measurement data obtained by field correlation remeasurements based on homodyne detection. Whereas the above achievements are limited to Gaussian states, we also present the joint measurement statistics for the correlation measurement of non-Gaussian states and show how correlation measurements can improve the reconstruction of Fock states. Thus, we are opening a avenue to the investigation of quantum phenomena of light on an ultrafast time scale.

METHODS

Discretization and the calculation (subcycle) mode basis

To discretise the continuous Hilbert space of the free-space electromagnetic field, we introduce the subcycle mode basis,

$$f_i(\omega) = f_0(\omega)\tilde{L}_i(\omega), \tag{11}$$

with two parameters, $\sigma_0, k_0 > 0$ based on the fundamental mode in equation (1), centred at $\bar{\omega}_0 \approx \sigma_0\sqrt{k_0 + 1/\pi}$ with bandwidth $\Delta\omega_0 \approx \sqrt{2\ln(2)}\sigma_0$ and the (scaled) generalized Laguerre polynomials

$$\tilde{L}_i(\omega) = \left[\frac{\Gamma(i+1)\Gamma(k_0+1/2)}{\Gamma(i+k_0+1/2)}\right]^{\frac{1}{2}} L_i^{(k_0-1/2)}\left(\frac{\omega^2}{\sigma_0^2}\right). \tag{12}$$

We used $\sigma_0/(2\pi) = 100\,\mathrm{THz}$ and $k_0 = 0.5$. See Supplementary Note 1 for further details about the subcycle mode basis. Using the relation $\hat{a}(\omega) \approx \sum_{i=0}^{i_{\max}} f_i^*(\omega)\hat{a}_i$, we can discretize the quadrature operator,

$$\hat{q}(0,0,\varphi') \approx \int_0^\infty \left[e^{\mathrm{i}\varphi'}\alpha_{\mathrm{LO}}(\omega)\{\hat{a}'_s(\omega)\}^\dagger + \mathrm{e}^{-\mathrm{i}\varphi'}\alpha^*_{\mathrm{LO}}(\omega)\hat{a}'_s(\omega)\right]\mathrm{d}\omega, \tag{13}$$

measured in a homodyne detection with a local oscillator described by a frequency-dependent coherent amplitude $\alpha_{\mathrm{LO}}(\omega)$ given by the function defined in equation (1) with parameters σ_{LO} and k_{LO} and a phase shift φ' due to a Φ-wave plate rotated by θ. By choosing

$$\theta = \frac{1}{2}\arccos\left(\sqrt{\frac{1-2\cos^2(\Phi/2)}{2\sin^2(\Phi/2)}}\right), \tag{14}$$

the effective phase can be calculated using

$$\varphi' = -\arctan\left(\sqrt{\frac{2\cos^2(\Phi/2)}{1-2\cos^2(\Phi/2)}}\right). \tag{15}$$

A detailed derivation is given in Supplementary Note 2. We collect the coefficients resulting from the mode expansion in the vector $\boldsymbol{\zeta}_{\mathrm{LO}}$, with

$$[\boldsymbol{\zeta}_{\mathrm{LO}}]_i = \begin{cases} \mathrm{Re}\left[\int_0^\infty \alpha_{\mathrm{LO}}(\omega) f_i(\omega)\mathrm{d}\omega\right] & 0 \le i < i_{\max} \\ \mathrm{Im}\left[\int_0^\infty \alpha_{\mathrm{LO}}(\omega) f_{i-i_{\max}}(\omega)\mathrm{d}\omega\right] & i_{\max} \le i < 2i_{\max} \end{cases}. \tag{16}$$

With

$$M_{\mathrm{WP}}(\varphi') = \begin{pmatrix} \cos(\varphi')\mathbb{I} & -\sin(\varphi')\mathbb{I} \\ \sin(\varphi')\mathbb{I} & \cos(\varphi')\mathbb{I} \end{pmatrix} \tag{17}$$

describing the effect of the wave plate, the measured quadrature can be expressed as

$$\hat{q} = \left(M_{\mathrm{WP}}^{\mathsf{T}}(\varphi')\boldsymbol{\zeta}_{\mathrm{LO}}\right)^{\mathsf{T}} \hat{\boldsymbol{\zeta}}. \tag{18}$$

The vector of mode operators $\hat{\boldsymbol{\zeta}}$ is defined in the introduction. With the matrix elements $\tilde{\omega}_{ij} = \int_0^\infty \omega f_i(\omega) f_j(\omega)\mathrm{d}\omega$ of the free-field Hamiltonian and the definition

$$G_{\Delta t} = \Delta t \begin{pmatrix} 0 & \tilde{\omega} \\ -\tilde{\omega} & 0 \end{pmatrix} \tag{19}$$

we can describe the time delay using the symplectic matrix $M_{\mathrm{DLY}}(\Delta t) = \exp(G_{\Delta t})$. The effect of the nonlinear crystal can be described with a squeezing and beam-splitting interaction of photons at (angular) frequency Ω and ω, using the kernels derived in the Supplementary Notes 3 and 4,

$$S(\Omega,\omega) = \frac{1}{\hbar}(2\pi)^{3/2}\left(\frac{\hbar}{4\pi\varepsilon_0 cA}\right)^{3/2}\sqrt{\frac{\omega+\Omega}{n(\omega+\Omega)}} f_\alpha(\omega+\Omega)\sqrt{\frac{\omega\Omega}{n(\omega)n(\Omega}}\widehat{\lambda}[\Delta k(\Omega,\omega)], \tag{20}$$

$$B(\Omega,\omega) = \frac{1}{\hbar}(2\pi)^{3/2}\left(\frac{\hbar}{4\pi\varepsilon_0 cA}\right)^{3/2}\sqrt{\frac{|\omega-\Omega|}{n(\omega+\Omega)}}\left[f_\alpha^*(\omega-\Omega)+f_\alpha(\Omega-\omega)\right]\sqrt{\frac{\omega\Omega}{n(\omega)n(\Omega}}\widehat{\lambda}[\Delta k(-\Omega,\omega)], \tag{21}$$

with c, $\hbar$, ε_0 being the speed of light in vacuum, reduced Planck constant, and the vacuum permittivity. Furthermore, $A = \pi(3\,\mu\mathrm{m})^2$ is the beam waist area and $\widehat{\lambda}[\Delta k(\Omega,\omega)]$ the Fourier transform of the transversal profile of the $\chi^{(2)}$ interaction at the wave-vector mismatch $\Delta k(\Omega,\omega)$. In case of a zinc-telluride crystal of length $L = 20\,\mu\mathrm{m}$ in free space, we have $\widehat{\lambda}(k) = \lambda\frac{L}{\sqrt{2\pi}}\mathrm{sinc}(kL/2)$ with $\lambda = A\varepsilon_0 d/2$, the interaction parameter $d = -n^4(\langle\omega\rangle)r_{41}$ and the electro-optic coefficient of zinc telluride [92], $r_{41} = 4\,\mathrm{pm\,V^{-1}}$. The refractive index $n(\omega)$ is modelled from experimental data [93]. The function $f_\alpha(\omega)$ described the spectrum of the coherent pump/probe pulse with amplitude α driving the nonlinear interaction. We assume the spectrum to be described by equation (1) with parameters $\sigma_p = 100\,\mathrm{THz}$ and $k_p = 4$. Expanding the kernel again in the subcycle mode basis leads to the matrix elements,

$$S_{ij} = 2\iint_0^\infty S(\Omega,\omega) f_i^*(\Omega) f_j^*(\omega)\mathrm{d}\Omega\mathrm{d}\omega, \tag{22}$$

$$B_{ij} = 2\iint_0^\infty B(\Omega,\omega) f_i(\Omega) f_j^*(\omega)\mathrm{d}\Omega\mathrm{d}\omega, \tag{23}$$

ARTICLE IN PRESS

and by defining the matrix

$$G_{\mathrm{NL}} = \begin{pmatrix} -\mathrm{Re}(S-B) & \mathrm{Im}(S-B) \\ \mathrm{Im}(S+B) & \mathrm{Re}(S+B) \end{pmatrix}, \tag{24}$$

we can describe the effect of the nonlinear interaction using the symplectic matrix $M_{\mathrm{NL}}(\alpha) = \exp[|\alpha| G_{\mathrm{NL}}]$. Applying the transformation of the beam splitter to the measured quadrature, we obtain equation (3).

Correlation analysis

Since the detection takes place at two outputs of a beam splitter, the detected modes commute and the operators $\mathbf{q} = (\hat{q}_a[\Delta t_a, 0, 0], \hat{q}_a[\Delta t_a, 0, \pi/2], \hat{q}_b[\Delta t_b, 0, 0], \hat{q}_b[\Delta t_b, 0, \pi/2])^{\mathsf{T}} / (\sqrt{2}\|\boldsymbol{\zeta}_{\mathrm{LO}}(0,0,0)\|)$ define a covariance matrix,

$$[\mathrm{cov}_{\hat{\rho},\mathrm{d}}]_{ij} = \frac{1}{2} \langle \{\mathbf{q}_i, \mathbf{q}_j\} \rangle_{\hat{\rho} \otimes |\mathrm{vac}\rangle\langle\mathrm{vac}|}, \tag{25}$$

corresponding to a valid quantum state, which we call the detected state. The von Neumann entropy [33] of the sampled state can be calculated from the symplectic spectrum $\{\nu_i\}_{i=1,2}$ using $S(\mathrm{cov}_{\hat{\rho},\mathrm{d}}) = \sum_{i=1}^{2} s(\nu_i)$ with

$$s(x) = \left(\frac{x+1}{2}\right) \log_2 \left(\frac{x+1}{2}\right) - \left(\frac{x-1}{2}\right) \log_2 \left(\frac{x-1}{2}\right). \tag{26}$$

Correlation measures can be calculated using the bipartition between the mode measured at arm a and b. Thus, the subsystem A is spanned by the mode operators in $\mathbf{q}_A = (\hat{q}_a[\Delta t_a, 0, 0], \hat{q}_a[\Delta t_a, 0, \pi/2])^{\mathsf{T}}$, and the subsystem B by $\mathbf{q}_B = (\hat{q}_b[\Delta t_b, 0, 0], \hat{q}_b[\Delta t_b, 0, \pi/2])^{\mathsf{T}}$. Moreover, by defining the time-reversal operator for the subsystem B, $\Lambda = \mathrm{diag}(1, 1, 1, -1)$, the logarithmic negativity,

$$L(\mathrm{cov}_{\hat{\rho},\mathrm{d}}) = \max\{0, -\log_2(\min\{\tilde{\nu}_i\}_{i=1,2})\}, \tag{27}$$

can be calculated from the symplectic spectrum $\{\tilde{\nu}_i\}_{i=1,2}$ of the covariance matrix $\Lambda \mathrm{cov}_{\hat{\rho},\mathrm{d}} \Lambda$ [33, 94]. The same bipartitian is used to calculate the quantum discord [95].

While not being independent of the local oscillator mode, analysing correlations in the time domain could offer insights to the entanglement of Gaussian states beyond correlations in the orthogonal mode basis and could be used to define a mode independent notion of entanglement present in Gaussian quantum states [96].

The joint probability distribution

A detailed derivation of the full joint measurement statistics of correlation homodyne detection (i.e., $\alpha_{\mathrm{DX}} = 0$) is given in the Supplementary Note 10. With the definitions

$$P_{\mathrm{LO}} = \boldsymbol{\zeta}_{\mathrm{LO}}(\Delta t_a, \pi/2)[\boldsymbol{\zeta}_{\mathrm{LO}}(\Delta t_a, \pi/2)]^{\mathsf{T}} + \boldsymbol{\zeta}_{\mathrm{LO}}(\Delta t_b, 0)[\boldsymbol{\zeta}_{\mathrm{LO}}(\Delta t_b, 0)]^{\mathsf{T}}, \tag{28}$$

and

$$\boldsymbol{\zeta}_d(x_a, p_b) = 4 \frac{P_{\mathrm{LO}}[x_a \boldsymbol{\zeta}_{\mathrm{LO}}(\Delta t_a, \pi/2) - p_b \boldsymbol{\zeta}_{\mathrm{LO}}(\Delta t_b, 0)]}{\|\boldsymbol{\zeta}_{\mathrm{LO}}(\Delta t_a, \pi/2) - \boldsymbol{\zeta}_{\mathrm{LO}}(\Delta t_b, 0)\|^2}, \tag{29}$$

as well as the covariance matrix (Ω defining the symplectic matrices)

$$\mathrm{cov}_\mathrm{d}^{-1} = 4\frac{\Omega^\mathsf{T} P_\mathrm{LO}^2 \Omega}{\|\boldsymbol{\zeta}_\mathrm{LO}(\Delta t_a, \pi/2) - \boldsymbol{\zeta}_\mathrm{LO}(\Delta t_b, 0)\|^2}, \tag{30}$$

we can express the integration kernel in equation (10) as

$$K(x_a, p_b|\boldsymbol{\zeta}) = \frac{2\sqrt{2}\exp\left[-2\frac{\|x_a\boldsymbol{\zeta}_\mathrm{LO}(\Delta t_a,\pi/2)-p_b\boldsymbol{\zeta}_\mathrm{LO}(\Delta t_b,0)\|^2}{\|\boldsymbol{\zeta}_\mathrm{LO}(\Delta t_a,\pi/2)-\boldsymbol{\zeta}_\mathrm{LO}(\Delta t_b,0)\|^2}\right]}{\|\boldsymbol{\zeta}_\mathrm{LO}(\Delta t_a, \pi/2) - \boldsymbol{\zeta}_\mathrm{LO}(\Delta t_b, 0)\|} \exp\left[\boldsymbol{\zeta}_\mathrm{d}^\mathsf{T}(x_a, p_b)\boldsymbol{\zeta} - \frac{1}{2}\boldsymbol{\zeta}^\mathsf{T}\,\mathrm{cov}_\mathrm{d}^{-1}\,\boldsymbol{\zeta}\right]. \tag{31}$$

We assume the quantum pulse is an n_ph-photon Fock state in a single temporal mode with mode function according to equation (1) parametrized by $\Delta\omega_\mathrm{ph} = 59\,\mathrm{THz}$ and $\bar{\omega}_\mathrm{ph}/(2\pi) = 202\,\mathrm{THz}$ ($k_\mathrm{ph} = 16$). By defining the projector P_ph of the Fock states phase space, we can calculate the Schur complement

$$\mathrm{cov}_\mathrm{schur}^{-1} = P_\mathrm{ph}(\mathrm{cov}_\mathrm{vac}^{-1} + \mathrm{cov}_\mathrm{d}^{-1})P_\mathrm{ph} - P_\mathrm{ph}\,\mathrm{cov}_\mathrm{d}^{-1}\,P_\mathrm{r}[P_\mathrm{r}(\mathrm{cov}_\mathrm{vac}^{-1} + \mathrm{cov}_\mathrm{d}^{-1})P_\mathrm{r}]^{-1}P_\mathrm{r}\,\mathrm{cov}_\mathrm{d}^{-1}\,P_\mathrm{ph}, \tag{32}$$

with singular values σ_x, σ_p and define

$$\boldsymbol{\zeta}_\mathrm{d,ph}(x_a, p_b) = P_\mathrm{ph}[\mathbb{I} - \mathrm{cov}_\mathrm{d}^{-1}\,P_\mathrm{r}\{P_\mathrm{r}(\mathrm{cov}_\mathrm{vac}^{-1} + \mathrm{cov}_\mathrm{d}^{-1})P_\mathrm{r}\}^{-1}P_\mathrm{r}]\boldsymbol{\zeta}_\mathrm{d}(x_a, p_b). \tag{33}$$

as well as the normalization envelope

$$N(x_a, p_a) = \frac{2\sqrt{2}\exp\left[-2\frac{\|x_a\boldsymbol{\zeta}_\mathrm{LO}(\Delta t_a,\pi/2)-p_b\boldsymbol{\zeta}_\mathrm{LO}(\Delta t_b,0)\|^2}{\|\boldsymbol{\zeta}_\mathrm{LO}(\Delta t_a,\pi/2)-\boldsymbol{\zeta}_\mathrm{LO}(\Delta t_b,0)\|^2}\right]}{\|\boldsymbol{\zeta}_\mathrm{LO}(\Delta t_a, \pi/2) - \boldsymbol{\zeta}_\mathrm{LO}(\Delta t_b, 0)\|}$$
$$\times \sqrt{\frac{(2\pi)^{2(i_\mathrm{max}-1)}}{\det\left(P_\mathrm{r}[\mathrm{cov}_\mathrm{vac}^{-1} + \mathrm{cov}_\mathrm{d}^{-1}]P_\mathrm{r}\right)}} \exp\left[\frac{1}{2}\boldsymbol{\zeta}_\mathrm{d}^\mathsf{T}(x_a, p_b)\Omega P_\mathrm{r}\{P_\mathrm{r}(\mathrm{cov}_\mathrm{vac}^{-1} + \mathrm{cov}_\mathrm{d}^{-1})P_\mathrm{r}\}^{-1}P_\mathrm{r}\Omega^\mathsf{T}\boldsymbol{\zeta}_\mathrm{d}(x_a, p_b)\right], \tag{34}$$

to express the probability distribution of the joint quadrature measurement of the Fock state as

$$\mathrm{Prob}(x_a, p_b) = N(x_a, p_b)\frac{(-1)^n}{\pi}\sqrt{\frac{2\pi}{\sigma_x}}\sqrt{\frac{2\pi}{\sigma_p}}\mathrm{e}^{\frac{[\boldsymbol{\zeta}_\mathrm{d,ph}^\mathsf{T}(x_a,p_b)\mathbf{e}_x]^2}{2\sigma_x}}\mathrm{e}^{\frac{[\boldsymbol{\zeta}_\mathrm{d,ph}^\mathsf{T}(x_a,p_b)\mathbf{e}_p]^2}{2\sigma_p}}$$
$$\times \sum_{i=0}^{n}\left(1-\frac{4}{\sigma_x}\right)^i\left(1-\frac{4}{\sigma_p}\right)^{n-i} L_i^{(-\frac{1}{2})}\left[2\frac{\{\boldsymbol{\zeta}_\mathrm{d,ph}^\mathsf{T}(x_a, p_b)\mathbf{e}_x\}^2}{\sigma_x^2 - 4\sigma_x}\right] L_{n-i}^{(-\frac{1}{2})}\left[2\frac{\{\boldsymbol{\zeta}_\mathrm{d,ph}^\mathsf{T}(x_a, p_b)\mathbf{e}_p\}^2}{\sigma_p^2 - 4\sigma_p}\right]. \tag{35}$$

If a finite quantum efficiency, η, of the detectors [43] is assumed, we have to replace the detection covariance matrix $\mathrm{cov}_\mathrm{d}^{-1}$ by $\frac{\eta}{2-\eta}\,\mathrm{cov}_\mathrm{d}^{-1}$ before calculating the singular values σ_q.

DATA AVAILABILITY

All data presented here is available online [89].

CODE AVAILABILITY

The Python code supporting the results can be obtained from the GitLab repository: https://gitlab.inf.uni-konstanz.de/emanuel.hubenschmid/subcycleq . A archived version of the specific code used here is available online [89].

ARTICLE IN PRESS

ARTICLE IN PRESS

REFERENCES

[1] R. E. Slusher, P. Grangier, A. LaPorta, B. Yurke, and M. J. Potasek, Pulsed squeezed light, Phys. Rev. Lett. **59**, 2566 (1987).

[2] T. Hirano and M. Matsuoka, Broadband squeezing of light by pulse excitation, Opt. Lett. **15**, 1153 (1990).

[3] D. T. Smithey, M. Beck, M. Belsley, and M. G. Raymer, Sub-shot-noise correlation of total photon number using macroscopic twin pulses of light, Phys. Rev. Lett. **69**, 2650 (1992).

[4] J. Gulla, K. Ryen, and J. Skaar, Limits for realizing single photons (2021), arXiv:2109.06472 [quant-ph].

[5] R. Yanagimoto, E. Ng, M. Jankowski, R. Nehra, T. P. McKenna, T. Onodera, L. G. Wright, R. Hamerly, A. Marandi, M. M. Fejer, and H. Mabuchi, Mesoscopic ultrafast nonlinear optics—the emergence of multimode quantum non-gaussian physics, Optica **11**, 896 (2024).

[6] S. L. Braunstein and P. van Loock, Quantum information with continuous variables, Rev. Mod. Phys. **77**, 513 (2005).

[7] C. Weedbrook, A. M. Lance, W. P. Bowen, T. Symul, T. C. Ralph, and P. K. Lam, Quantum cryptography without switching, Phys. Rev. Lett. **93**, 170504 (2004).

[8] A. M. Lance, T. Symul, V. Sharma, C. Weedbrook, T. C. Ralph, and P. K. Lam, No-switching quantum key distribution using broadband modulated coherent light, Phys. Rev. Lett. **95**, 180503 (2005).

[9] L. S. Madsen, V. C. Usenko, M. Lassen, R. Filip, and U. L. Andersen, Continuous variable quantum key distribution with modulated entangled states, Nat. Commun. **3**, 10.1038/ncomms2097 (2012).

[10] V. C. Usenko and F. Grosshans, Unidimensional continuous-variable quantum key distribution, Phys. Rev. A **92**, 062337 (2015).

[11] E. Diamanti and A. Leverrier, Distributing secret keys with quantum continuous variables: Principle, security and implementations, Entropy **17**, 6072 (2015).

[12] N. Hosseinidehaj, Z. Babar, R. Malaney, S. X. Ng, and L. Hanzo, Satellite-based continuous-variable quantum communications: State-of-the-art and a predictive outlook, IEEE Commun. Surv. Tutor. **21**, 881 (2019).

[13] C. Silberhorn, T. C. Ralph, N. Lütkenhaus, and G. Leuchs, Continuous variable quantum cryptography: Beating the 3 db loss limit, Physical Review Letters **89**, 167901 (2002).

[14] M. Hillery, Quantum cryptography with squeezed states, Physical Review A **61**, 022309 (2000).

[15] V. R. Christiansen, A. H. Kiilerich, and K. Mølmer, Interactions of quantum systems with pulses of quantized radiation: From a cascaded master equation to a traveling mode perspective, Physical Review A **107**, 013706 (2023).

[16] V. R. Christiansen, M. Middelhede Lund, F. Yang, and K. Mølmer, Jaynes-cummings interaction with a traveling light pulse, Journal of the Optical Society of America B **41**, C140 (2024).

[17] V. R. Christiansen and K. Mølmer, Interactions in quantum networks with pulse propagation delays (2025).

ARTICLE IN PRESS

ARTICLE IN PRESS

[18] A. Zavatta, M. Bellini, P. L. Ramazza, F. Marin, and F. T. Arecchi, Time-domain analysis of quantum states of light: noise characterization and homodyne tomography, J. Opt. Soc. Am. B. **19**, 1189 (2002).

[19] A. Zavatta, S. Viciani, and M. Bellini, Non-classical field characterization by high-frequency, time-domain quantum homodyne tomography, Laser Phys. Lett. **3**, 3 (2005).

[20] O. Haderka, V. Michálek, V. Urbášek, and M. Ježek, Fast time-domain balanced homodyne detection of light, Appl. Optics **48**, 2884 (2009).

[21] R. Okubo, M. Hirano, Y. Zhang, and T. Hirano, Pulse-resolved measurement of quadrature phase amplitudes of squeezed pulse trains at a repetition rate of 76 MHz, Opt. Lett. **33**, 1458 (2008).

[22] V. Ansari, G. Harder, M. Allgaier, B. Brecht, and C. Silberhorn, Temporal-mode measurement tomography of a quantum pulse gate, Phys. Rev. A **96**, 063817 (2017).

[23] J. Tiedau, V. S. Shchesnovich, D. Mogilevtsev, V. Ansari, G. Harder, T. J. Bartley, N. Korolkova, and C. Silberhorn, Quantum state and mode profile tomography by the overlap, New J. Phys. **20**, 033003 (2018).

[24] V. Ansari, J. M. Donohue, M. Allgaier, L. Sansoni, B. Brecht, J. Roslund, N. Treps, G. Harder, and C. Silberhorn, Tomography and purification of the temporal-mode structure of quantum light, Phys. Rev. Lett. **120**, 213601 (2018).

[25] J. Gil-Lopez, Y. S. Teo, S. De, B. Brecht, H. Jeong, C. Silberhorn, and L. L. Sánchez-Soto, Universal compressive tomography in the time-frequency domain, Optica **8**, 1296 (2021).

[26] M. Kalash and M. V. Chekhova, Wigner function tomography via optical parametric amplification, Optica **10**, 1142 (2023).

[27] L. Serino, J. Gil-Lopez, M. Stefszky, R. Ricken, C. Eigner, B. Brecht, and C. Silberhorn, Realization of a multi-output quantum pulse gate for decoding high-dimensional temporal modes of single-photon states, PRX Quantum **4**, 020306 (2023).

[28] S. Mrówczyński and B. Müller, Wigner functional approach to quantum field dynamics, Physical Review D **50**, 7542 (1994).

[29] F. S. Roux and N. Fabre, Wigner functional theory for quantum optics (2019).

[30] S. Virally and B. Reulet, Unidimensional time-domain quantum optics, Physical Review A **100**, 023833 (2019).

[31] F. S. Roux, Erratum: Combining spatiotemporal and particle-number degrees of freedom [phys. rev. a 98, 043841 (2018)], Physical Review A **101**, 019903 (2020).

[32] G. Adesso, S. Ragy, and A. R. Lee, Continuous variable quantum information: Gaussian states and beyond, Open Systems & Information Dynamics **21**, 1440001 (2014).

[33] C. Weedbrook, S. Pirandola, R. García-Patrón, N. J. Cerf, T. C. Ralph, J. H. Shapiro, and S. Lloyd, Gaussian quantum information, Reviews of Modern Physics **84**, 621 (2012).

[34] M. G. Raymer and I. A. Walmsley, Temporal modes in quantum optics: then and now, Physica Scripta **95**, 064002 (2020).

ARTICLE IN PRESS

ARTICLE IN PRESS

[35] B. Brecht, D. V. Reddy, C. Silberhorn, and M. G. Raymer, Photon temporal modes: A complete framework for quantum information science, Physical Review X **5**, 041017 (2015).

[36] M. Freyberger, K. Vogel, and W. P. Schleich, From photon counts to quantum phase, Phys. Lett. A **176**, 41 (1993).

[37] D. T. Smithey, M. Beck, J. Cooper, and M. G. Raymer, Measurement of number-phase uncertainty relations of optical fields, Phys. Rev. A **48**, 3159 (1993).

[38] U. Leonhardt and H. Paul, Realistic optical homodyne measurements and quasiprobability distributions, Phys. Rev. A **48**, 4598 (1993).

[39] A. Zucchetti, W. Vogel, and D.-G. Welsch, Quantum-state homodyne measurement with vacuum ports, Phys. Rev. A **54**, 856 (1996).

[40] J. Řeháček, Y. S. T., Z. Hradil, and S. Wallentowitz, Surmounting intrinsic quantum-measurement uncertainties in Gaussian-state tomography with quadrature squeezing, Sci. Rep. **5**, 10.1038/srep12289 (2015).

[41] E. Hubenschmid, T. L. M. Guedes, and G. Burkard, Complete positive operator-valued measure description of multichannel quantum electro-optic sampling with monochromatic field modes, Phys. Rev. A **106**, 043713 (2022).

[42] K. Vogel and H. Risken, Determination of quasiprobability distributions in terms of probability distributions for the rotated quadrature phase, Phys. Rev. A **40**, 2847 (1989).

[43] U. Leonhardt and H. Paul, High-accuracy optical homodyne detection with low-efficiency detectors: "preamplification" from antisqueezing, Phys. Rev. Lett. **72**, 4086 (1994).

[44] S. Wallentowitz and W. Vogel, Unbalanced homodyning for quantum state measurements, Phys. Rev. A **53**, 4528 (1996).

[45] A. Luis, J. Sperling, and W. Vogel, Nonclassicality phase-space functions: More insight with fewer detectors, Phys. Rev. Lett. **114**, 103602 (2015).

[46] M. Bohmann, J. Tiedau, T. Bartley, J. Sperling, C. Silberhorn, and W. Vogel, Incomplete detection of nonclassical phase-space distributions, Phys. Rev. Lett. **120**, 063607 (2018).

[47] E. Knyazev, K. Y. Spasibko, M. V. Chekhova, and F. Y. Khalili, Quantum tomography enhanced through parametric amplification, New J. Phys. **20**, 013005 (2018).

[48] S. Olivares, A. Allevi, G. Caiazzo, M. G. A. Paris, and M. Bondani, Quantum tomography of light states by photon-number-resolving detectors, New J. Phys. **21**, 103045 (2019).

[49] D. T. Smithey, M. Beck, M. G. Raymer, and A. Faridani, Measurement of the Wigner distribution and the density matrix of a light mode using optical homodyne tomography: Application to squeezed states and the vacuum, Phys. Rev. Lett. **70**, 1244 (1993).

[50] E. Hubenschmid, T. L. M. Guedes, and G. Burkard, Optical time-domain quantum state tomography on a subcycle scale, Physical Review X **14**, 041032 (2024).

ARTICLE IN PRESS

ARTICLE IN PRESS

[51] G. Yang, M. Kizmann, A. Leitenstorfer, and A. S. Moskalenko, Subcycle tomography of quantum light (2023), arXiv:2307.12812 [quant-ph].

[52] S. Onoe, S. Virally, and D. V. Seletskiy, Direct measurement of the husimi-q function of the electric-field in the time-domain (2023), arXiv:2307.13088 [quant-ph].

[53] N. Lordi, E. J. Tsao, A. J. Lind, S. A. Diddams, and J. Combes, Quantum theory of temporally mismatched homodyne measurements with applications to optical-frequency-comb metrology, Physical Review A **109**, 033722 (2024).

[54] C. Riek, D. V. Seletskiy, A. S. Moskalenko, J. F. Schmidt, P. Krauspe, S. Eckart, S. Eggert, G. Burkard, and A. Leitenstorfer, Direct sampling of electric-field vacuum fluctuations, Science **350**, 420 (2015).

[55] A. S. Moskalenko, C. Riek, D. V. Seletskiy, G. Burkard, and A. Leitenstorfer, Paraxial theory of direct electro-optic sampling of the quantum vacuum, Phys. Rev. Lett. **115**, 263601 (2015).

[56] M. Kizmann, A. S. Moskalenko, A. Leitenstorfer, G. Burkard, and S. Mukamel, Quantum susceptibilities in time-domain sampling of electric field fluctuations, Laser Photonics Rev. **16**, 2100423 (2022).

[57] S. Onoe, T. L. M. Guedes, A. S. Moskalenko, A. Leitenstorfer, G. Burkard, and T. C. Ralph, Realizing a rapidly switched Unruh-DeWitt detector through electro-optic sampling of the electromagnetic vacuum, Phys. Rev. D **105**, 056023 (2022).

[58] T. L. M. Guedes, I. Vakulchyk, D. V. Seletskiy, A. Leitenstorfer, A. S. Moskalenko, and G. Burkard, Back action in quantum electro-optic sampling of electromagnetic vacuum fluctuations, Phys. Rev. Research **5**, 013151 (2023).

[59] F. Lindel, R. Bennett, and S. Y. Buhmann, Macroscopic quantum electrodynamics approach to nonlinear optics and application to polaritonic quantum-vacuum detection, Phys. Rev. A **103**, 033705 (2021).

[60] I.-C. Benea-Chelmus, J. Faist, A. Leitenstorfer, A. S. Moskalenko, I. Pupeza, D. V. Seletskiy, and K. L. Vodopyanov, Electro-optic sampling of classical and quantum light, Optica **12**, 546 (2025).

[61] C. Riek, P. Sulzer, M. Seeger, A. S. Moskalenko, G. Burkard, D. V. Seletskiy, and A. Leitenstorfer, Subcycle quantum electrodynamics, Nature **541**, 376 (2017).

[62] M. Kizmann, T. L. M. Guedes, D. V. Seletskiy, A. S. Moskalenko, A. Leitenstorfer, and G. Burkard, Subcycle squeezing of light from a time flow perspective, Nat. Phys. **15**, 960 (2019).

[63] T. L. M. Guedes, M. Kizmann, D. V. Seletskiy, A. Leitenstorfer, G. Burkard, and A. S. Moskalenko, Spectra of ultrabroadband squeezed pulses and the finite-time Unruh-Davies effect, Phys. Rev. Lett. **122**, 053604 (2019).

[64] S. Namba, Electro-optical effect of zincblende, J. Opt. Soc. Am. **51**, 76 (1961).

[65] G. Gallot and D. Grischkowsky, Electro-optic detection of terahertz radiation, J. Opt. Soc. Am. B. **16**, 1204 (1999).

[66] A. Leitenstorfer, S. Hunsche, J. Shah, M. C. Nuss, and W. H. Knox, Detectors and sources for ultrabroadband electro-optic sampling: Experiment and theory, Appl. Phys. Lett. **74**, 1516 (1999).

ARTICLE IN PRESS

ARTICLE IN PRESS

[67] H. Kempf, A. Muraviev, F. Breuning, P. G. Schunemann, R. Tenne, A. Leitenstorfer, and K. Vodopyanov, Direct sampling of femtosecond electric-field waveforms from an optical parametric oscillator, APL Photonics **9**, 10.1063/5.0189059 (2024).

[68] C. Beckh, P. Sulzer, N. Fritzsche, C. Riek, and A. Leitenstorfer, Analysis of subcycle electro-optic sampling without background, J Infrared Millim Terahertz Waves **42**, 701 (2021).

[69] O. Schubert, M. Hohenleutner, F. Langer, B. Urbanek, C. Lange, U. Huttner, D. Golde, T. Meier, M. Kira, S. W. Koch, and R. Huber, Sub-cycle control of terahertz high-harmonic generation by dynamical bloch oscillations, Nature Photonics **8**, 119 (2014).

[70] F. Langer, M. Hohenleutner, C. P. Schmid, C. Poellmann, P. Nagler, T. Korn, C. Schüller, M. S. Sherwin, U. Huttner, J. T. Steiner, S. W. Koch, M. Kira, and R. Huber, Lightwave-driven quasiparticle collisions on a subcycle timescale, Nature **533**, 225 (2016).

[71] S. Virally, P. Cusson, and D. V. Seletskiy, Enhanced electro-optic sampling with quantum probes, Phys. Rev. Lett. **127**, 270504 (2021).

[72] P. Sulzer, K. Oguchi, J. Huster, M. Kizmann, T. L. M. Guedes, A. Liehl, C. Beckh, A. S. Moskalenko, G. Burkard, D. V. Seletskiy, and A. Leitenstorfer, Determination of the electric field and its Hilbert transform in femtosecond electro-optic sampling, Phys. Rev. A **101**, 033821 (2020).

[73] D. A. Kopylov, T. Meier, and P. R. Sharapova, Theory of multimode squeezed light generation in lossy media (2024).

[74] B. Yurke and J. S. Denker, Quantum network theory, Physical Review A **29**, 1419 (1984).

[75] N. G. Walker and J. E. Carroll, Multiport homodyne detection near the quantum noise limit, Opt. Quant. Electron. **18**, 355 (1986).

[76] G. Breitenbach, S. Schiller, and J. Mlynek, Measurement of the quantum states of squeezed light, Nature **387**, 471 (1997).

[77] I.-C. Benea-Chelmus, F. F. Settembrini, G. Scalari, and J. Faist, Electric field correlation measurements on the electromagnetic vacuum state, Nature **568**, 202 (2019).

[78] F. Lindel, R. Bennett, and S. Y. Buhmann, Theory of polaritonic quantum-vacuum detection, Physical Review A **102**, 041701 (2020).

[79] F. F. Settembrini, F. Lindel, A. M. Herter, S. Y. Buhmann, and J. Faist, Detection of quantum-vacuum field correlations outside the light cone, Nat. Commun. **13**, 10.1038/s41467-022-31081-1 (2022).

[80] F. F. Settembrini, A. Herter, and J. Faist, Third order nonlinear correlation of the electromagnetic vacuum at near-infrared frequencies (2023).

[81] F. Lindel, A. M. Herter, J. Faist, and S. Y. Buhmann, Probing vacuum field fluctuations and source radiation separately in space and time, Physical Review Research **5**, 043207 (2023).

[82] F. Lindel, A. Herter, V. Gebhart, J. Faist, and S. Y. Buhmann, Entanglement harvesting from electromagnetic quantum fields, Physical Review A **110**, 022414 (2024).

ARTICLE IN PRESS

ARTICLE IN PRESS

[83] M. A. Weiss, A. Herbst, J. Schlegel, T. Dannegger, M. Evers, A. Donges, M. Nakajima, A. Leitenstorfer, S. T. B. Goennenwein, U. Nowak, and T. Kurihara, Discovery of ultrafast spontaneous spin switching in an antiferromagnet by femtosecond noise correlation spectroscopy, Nature Communications **14**, 10.1038/s41467-023-43318-8 (2023).

[84] D. F. McAlister and M. G. Raymer, Correlation and joint density matrix of two spatial–temporal modes from balanced-homodyne sampling, Journal of Modern Optics **44**, 2359 (1997).

[85] D. F. McAlister and M. G. Raymer, Ultrafast photon-number correlations from dual-pulse, phase-averaged homodyne detection, Physical Review A **55**, R1609 (1997).

[86] G. Yang, S. Sharma, and A. S. Moskalenko, Electro-optic sampling of the electric-field operator for ultrabroadband pulses of gaussian quantum light, Quantum Science and Technology **10**, 045033 (2025).

[87] E. H. Moore, On the reciprocal of the general algebraic matrix, Bulletin of the American Mathematical Society **26**, 394 (1920).

[88] R. Penrose, A generalized inverse for matrices, Mathematical Proceedings of the Cambridge Philosophical Society **51**, 406 (1955).

[89] E. Hubenschmid, Subcycleq (2025).

[90] O. Tziperman, V. R. Christiansen, I. Kaminer, and K. Mølmer, Parametric amplification of a quantum pulse, Physical Review A **110**, 053712 (2024).

[91] A. I. Lvovsky, H. Hansen, T. Aichele, O. Benson, J. Mlynek, and S. Schiller, Quantum state reconstruction of the single-photon fock state, Physical Review Letters **87**, 050402 (2001).

[92] R. W. Boyd, *Nonlinear optics* (Elsevier Science & Technology, 2019).

[93] D. T. F. Marple, Refractive index of ZnSe, ZnTe, and CdTe, J. Appl. Phys. **35**, 539 (1964).

[94] G. Adesso, A. Serafini, and F. Illuminati, Extremal entanglement and mixedness in continuous variable systems, Physical Review A **70**, 022318 (2004).

[95] G. Adesso and A. Datta, Quantum versus classical correlations in gaussian states, Physical Review Letters **105**, 030501 (2010).

[96] J. Sperling, A. Perez-Leija, K. Busch, and C. Silberhorn, Mode-independent quantum entanglement for light, Physical Review A **100**, 062129 (2019).

ARTICLE IN PRESS

ACKNOWLEDGMENTS

We acknowledge funding by the Deutsche Forschungsgemeinschaft (DFG) - Project No. 425217212 - SFB 1432.

ARTICLE IN PRESS

AUTHOR CONTRIBUTIONS

E.H. performed the calculations and wrote the manuscript. G.B. improved the manuscript and supervised the project.

COMPETING INTERESTS

The authors declare no competing interests.

ARTICLE IN PRESS

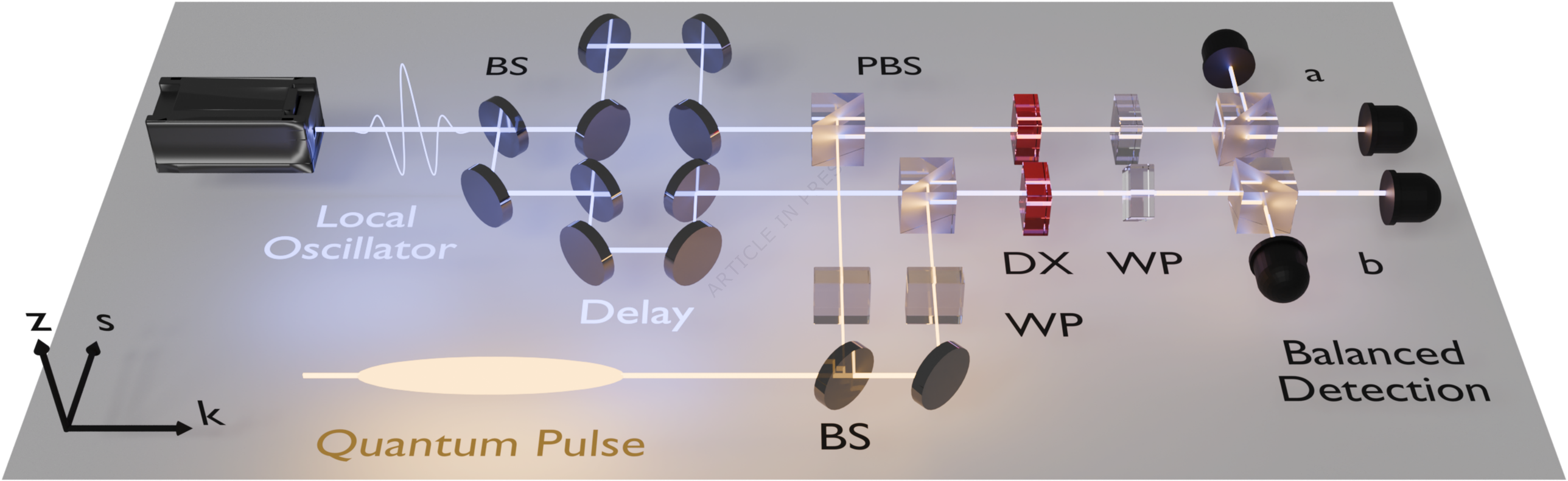
BS
PBS
a
Local
Oscillator
DX
WP
b
Delay
WP
z
s
Balanced
Detection
k
Quantum Pulse
BS

ARTICLE IN PRESS

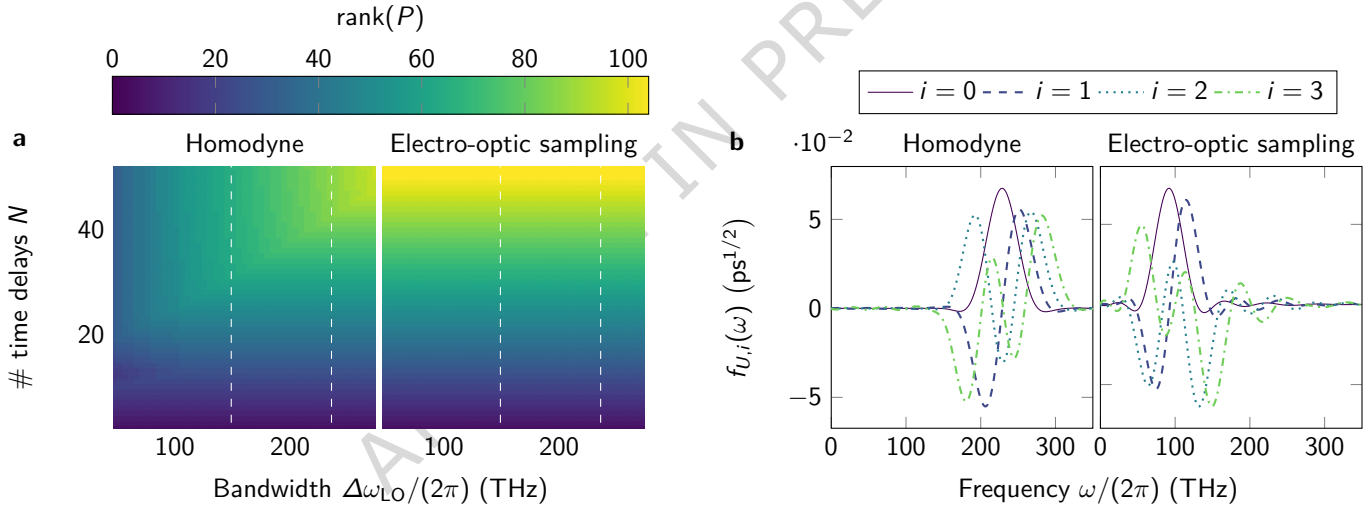

ARTICLE IN PRESS

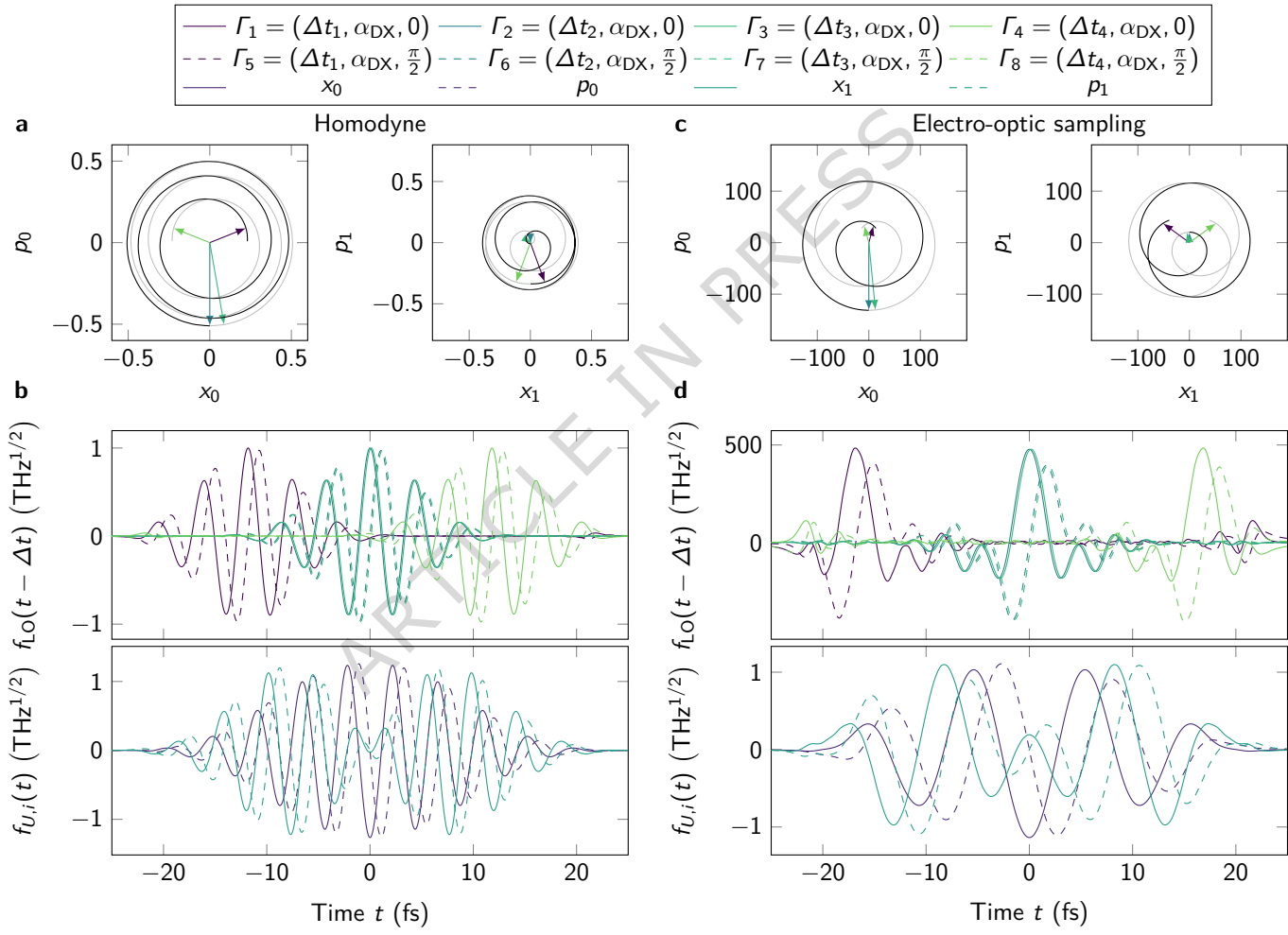

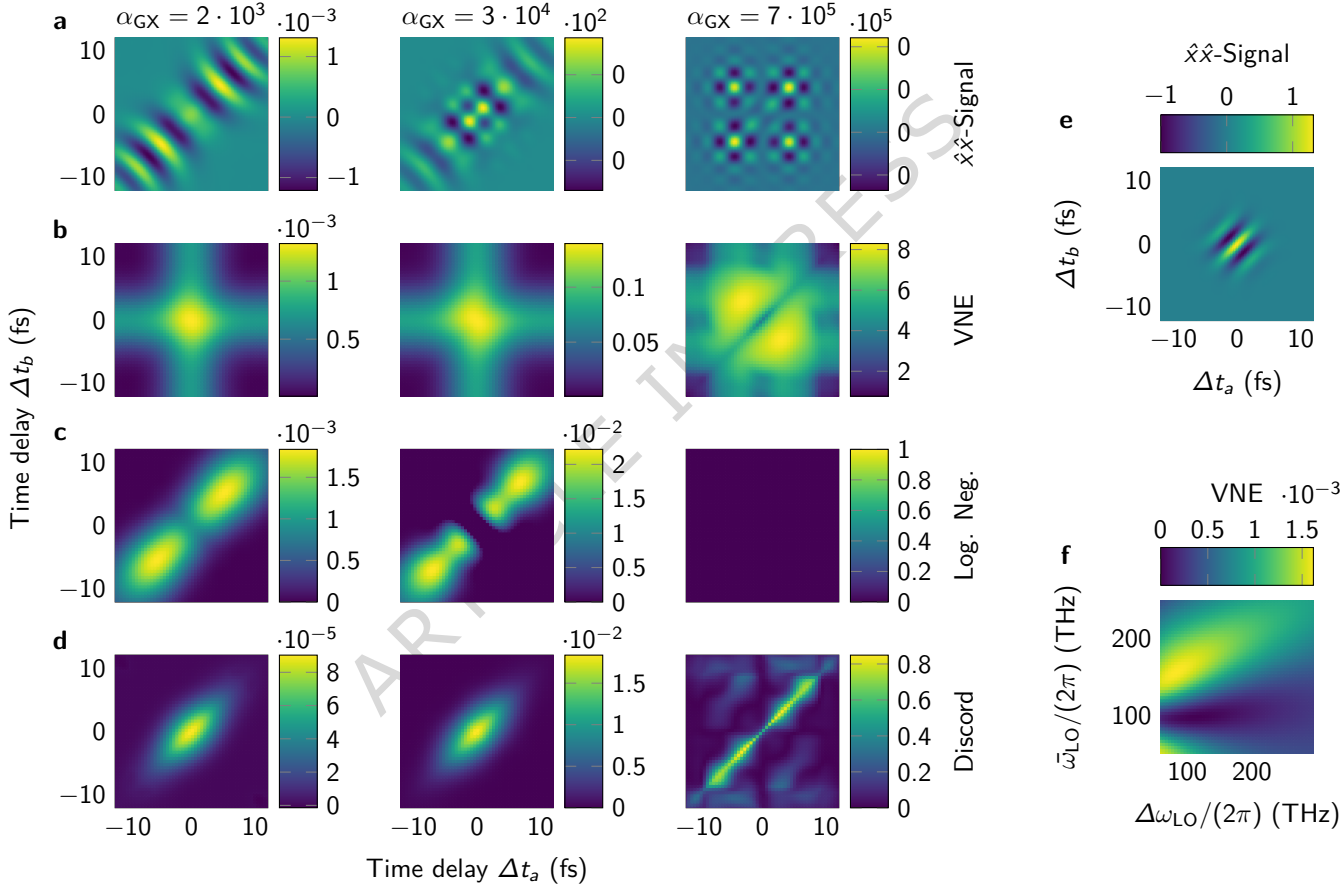

ARTICLE IN PRESS

ARTICLE IN PRESS